Directional Frame Timing Synchronization in Wideband Millimeter-Wave Systems with Low-Resolution ADCs

Dalin Zhu, Ralf Bendlin, Salam Akoum, Arunabha Ghosh, and Robert W. Heath, Jr.

Abstract—In this paper, we propose and evaluate a novel beamforming strategy for directional frame timing synchronization in wideband millimeter-wave (mmWave) systems operating with low-resolution analog-to-digital converters (ADCs). In the employed system model, we assume multiple radio frequency chains equipped at the base station to simultaneously form multiple synchronization beams in the analog domain. We formulate the corresponding directional frame timing synchronization problem as a max-min multicast beamforming problem under low-resolution quantization. We first show that the formulated problem cannot be effectively solved by conventional singlestream beamforming based approaches due to large quantization loss and limited beam codebook resolution. We then develop a new multi-beam probing based directional synchronization strategy, targeting at maximizing the minimum received synchronization signal-to-quantization-plus-noise ratio (SQNR) among all users. Leveraging a common synchronization signal structure design, the proposed approach synthesizes an effective composite beam from the simultaneously probed beams to better trade off the beamforming gain and the quantization distortion. Numerical results reveal that for wideband mmWave systems with lowresolution ADCs, the timing synchronization performance of our proposed method outperforms the existing approaches due to the improvement in the received synchronization SQNR.

I. INTRODUCTION

The millimeter-wave (mmWave) band offers high data rates in both wireless local area networks [2] and fifth-generation (5G) mobile cellular systems [3]. As mmWave systems make use of large available bandwidths, the corresponding sampling rate of the analog-to-digital converters (ADCs) scales up, which results in high power consumption and hardware implementation complexity. It is desirable to reduce the ADCs' resolution in mmWave systems to reduce implementation costs. The use of low-resolution ADCs in wireless communications systems has been investigated in various aspects [4]-[8], but most of the prior work on low-resolution ADCs focused on analytical performance assessment rather than practical implementation issues such as synchronization.

Dalin Zhu is with Samsung Research America, Plano, TX, 75023 USA, e-mail: dalin.zhu@samsung.com.

Robert W. Heath, Jr. is with the Department of Electrical and Computer Engineering, The University of Texas at Austin, Austin, TX, 78712 USA, e-mail: rheath@utexas.edu.

Ralf Bendlin, Salam Akoum and Arunabha Ghosh are with AT&T Labs, Austin, TX, 78759 USA, e-mail: {ralf_bendlin, salam_akoum, ghosh}@labs.att.com.

Parts of this work have been presented at the IEEE Fifty-First Asilomar Conference on Signals, Systems and Computers [1]. This work was supported in part by the National Science Foundation under Grant No. ECCS-1711702, CNS-1702800 and CNS-1731658 and a gift from AT&T Labs.

Current lower-frequency cellular networks such as longterm evolution (LTE) systems [9] conduct frame timing synchronization using omni-directional transmission and reception. Directional transmission and detection of synchronization signals is interesting in mmWave systems due to the low signal-to-noise ratio (SNR) prior to beamforming [10]. For directional synchronization, the network sends synchronization signals towards predefined angular directions via beamforming [11]. In [12], a random beamforming (beams are formed towards randomly selected angular directions) based initial access process was proposed for mmWave systems. The analytical performance assessment, however, was the main focus of [12] withtout incorporating the effect of lowresolution quantization. In [13], a comb-type synchronization signal structure along with a generalized likelihood ratio test detection strategy was developed to facilitate the cell discovery in the absence of channel directional information; some preliminary simulation results assuming few-bit ADCs were provided, but the synchronization beams were not optimized for low-resolution quantization. In [14], low-resolution frequency synchronization was the design focus with custom designed synchronization sequences resistant to the quantization distortion.

In this paper, we propose and evaluate a new beamforming strategy to improve the frame timing synchronization performance for mmWave cellular systems under low-resolution ADCs. Different from our prior work in [1], in which the developed synchronization method mainly focused on a single user setup, the proposed approach in this paper incorporates multiple users and optimizes the overall synchronization performance. The idea of optimizing the beam pattern for lowresolution quantization was also proposed in [15], [16], but the prior work did not address any specific system design issues such as the frame timing synchronization problem considered in this paper. In our system model, the base station (BS) deploys multiple radio frequency (RF) chains and simultaneously forms multiple synchronization beams in the analog domain. Upon receiving the synchronization signals, the user equipment (UE) conducts cross-correlation based frame timing synchronization with fully digital front ends and low-resolution ADCs. We summarize the main contributions of the paper as follows:

 Optimization problem formulation for directional frame timing synchronization under low-resolution ADCs: For a single UE with low-resolution ADCs, we leverage

1

Bussgang's decomposition theorem [17], [18] to formulate the corresponding received synchronization signalto-quantization-plus-noise ratio (SQNR) at zero-lag correlation. This formulation accounts for both the spatial correlation brought by the directional beamforming and the inherent correlation of the employed synchronization signals. Building on the derivation of a single UE's synchronization SONR, we extend the problem formulation of low-resolution synchronization to a multi-user scenario. In this case, we focus on maximizing the minimum received synchronization SQNR at zero-lag correlation among all UEs. We show that this type of max-min multicast problem cannot be effectively solved by existing single-stream beamforming based approaches due to large quantization distortion and limited beam codebook resolution.

- New directional frame timing synchronization design under low-resolution ADCs: Without channel knowledge (a common assumption for synchronization), we first discretize the given angular range with a set of potential channel directions and transform the complex max-min multicast problem into a maximization problem. We then develop a new multi-beam probing based directional synchronization strategy to tackle this problem. Leveraging a common synchronization signal structure design, the simultaneously probed synchronization beams form an effective composite beam. We show that by optimizing the effective composite beam pattern, a good tradeoff between the beamforming gain and the resulted quantization distortion can be achieved, resulting in improved frame timing synchronization performance under low-resolution quantization.
- Practical implementation of proposed low-resolution timing synchronization: We introduce two resource allocation strategies for the synchronization signal, which are: (i) continuous subcarriers allocation, and (ii) comb-type subcarriers allocation. The comb-type assignment can better exploit frequency diversity of the propagation channel, but the continuous allocation is easier to implement. We also discuss necessary system statistics and longterm measurements required to further improve the timing synchronization performance of our proposed method.

We organize the rest of the paper as follows. In Section II, we specify the system and channel models for the directional frame timing synchronization design in mmWave systems. In Section III, we formulate the directional frame timing synchronization problem under low-resolution ADCs. In Section IV, we explicitly illustrate the design principle and procedure of the proposed multi-beam probing strategy. We evaluate the proposed synchronization method in Section V assuming both narrowband and wideband channels. We draw our conclusions in Section VI.

Notations: A (A) is a matrix; a (a) is a vector; a (a) is a scalar; |a| is the magnitude of the complex number a; $(\cdot)^{\mathrm{T}}$ and $(\cdot)^*$ denote transpose and conjugate transpose; $((\cdot))_N$ represents the modulo-N operation; $[A]_{:,j}$ is the j-th column of A; $[A]_{i,j}$ is the (i,j)-th entry of A; $[a]_j$ represents the j-th

element of $\boldsymbol{a}; [\boldsymbol{a}]_{j_1:j_2}$ contains elements j_1, j_1+1, \cdots, j_2 of $\boldsymbol{a}; [\boldsymbol{A}]_{:,j_1:j_2}$ contains columns j_1, j_1+1, \cdots, j_2 of $\boldsymbol{A}; \operatorname{tr}(\boldsymbol{A})$ is the trace of $\boldsymbol{A}; \boldsymbol{I}_N$ is the $N \times N$ identity matrix; $\mathbf{1}_{M \times N}$ represents the $M \times N$ matrix whose entries are all ones; $\mathbf{0}_N$ denotes the $N \times 1$ vector whose entries are all zeros; $\mathcal{N}_c(\boldsymbol{a}, \boldsymbol{A})$ is a complex Gaussian vector with mean \boldsymbol{a} and covariance $\boldsymbol{A}; \mathbb{E}[\cdot]$ is used to denote expectation; $\gcd(\cdot)$ is the greatest common divisor; the diagonal matrix $\operatorname{diag}(\boldsymbol{A})$ has $\left\{[\boldsymbol{A}]_{i,i}\right\}$ as its diagonal entries, and $\operatorname{diag}(\boldsymbol{a}^T)$ has $\left\{[\boldsymbol{a}]_j\right\}$ as its diagonal entries; and $\operatorname{diag}\left\{\cdot\right\}$ is the diagonalization operation.

II. SYSTEM AND CHANNEL MODELS

In this section, we introduce the system model for the directional frame timing synchronization design in mmWave systems. We also summarize the common wideband channel model.

A. System model for directional frame timing synchronization in mmWave systems

In this paper, we assume that the BS employs directional beams to transmit the downlink synchronization signals, providing sufficient link margin at mmWave frequencies. Note that the directional transmission of downlink synchronization signals will also be supported in the 3rd Generation Partnership Project (3GPP) 5G New Radio (NR) systems [11], [19]. In the following, we first present the assumed antenna array configurations and transceiver architecture along with the synchronization signal structure. We then develop the received synchronization signal model for our system. Finally, we explain the cross-correlation based frame timing synchronization design using the derived received signal model.

1) Transceiver architecture, array configurations and synchronization signal structure. We consider a precoded multiple-input multiple-output (MIMO) orthogonal frequency division multiplexing (OFDM) system with N subcarriers. The BS employs an array-of-subarray architecture with $N_{\rm tot}$ transmit antennas and $N_{\rm RF}$ RF chains, and the UE deploys fully digital front ends with $M_{\rm tot}$ receive antennas. In an array-of-subarray architecture, a single RF chain controls an antenna subarray. Denoting the number of antenna elements in each transmit subarray by $N_{\rm A}$, then $N_{\rm tot}=N_{\rm RF}N_{\rm A}$. Note that our proposed method in Section IV can be applied to other transceiver architectures with moderate modifications to the design procedure.

Due to their constant amplitude and zero autocorrelation in both the time and frequency domains [20], Zadoff-Chu (ZC)-type sequences are employed in this paper for the downlink synchronization signals. Denote the length of the employed ZC sequence by $N_{\rm ZC}$ and the sequence root index by i ($i \in \{1,\cdots,N_{\rm ZC}-1\}$ and $\gcd(N_{\rm ZC},i)=1$). For $m=0,\cdots,N_{\rm ZC}-1$, the sequence can be represented as

$$s_i[m] = \exp\left\{-\mathrm{j}\frac{\pi m(m+1)i}{N_{\mathrm{ZC}}}\right\}.$$
 (1)

The cyclic auto-correlation of the ZC sequence results in a single dirac-impulse at zero-lag correlation, i.e.,

$$\chi[v] = \sum_{m=0}^{N_{\rm ZC}-1} s_i[m] s_i^*[((m+v))_{N_{\rm ZC}}] = \delta[v],$$
 (2)

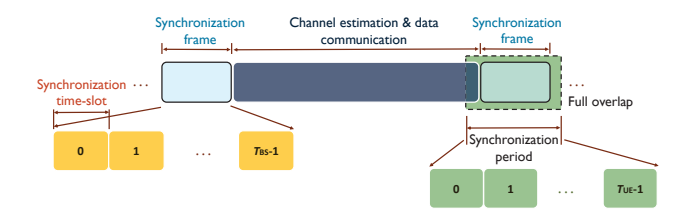


Fig. 1. A conceptual example of our synchronization frame structure. The BS-wise synchronization frame consists of $T_{\rm BS}$ synchronization time-slots. The length of one UE-wise synchronization period is equivalent to the duration of $T_{\rm UE}$ OFDM symbols. In this example, the synchronization signal samples sent during a given BS-wise synchronization frame can be fully detected by the UE via its synchronization period (full overlap).

$$v = 0, \cdots, N_{\rm ZC} - 1.$$

The UE can therefore use this property to detect the correct frame timing position. In practice, the channel variations, noise power, and other impairments will affect the actual correlation values. Especially under low-resolution quantization, the good correlation properties of the ZC sequence are severely deteriorated by the quantization distortion. Note that other sequences such as the Golay complementary sequences can also be used for frame timing synchronization as long as they exhibit a similar correlation property to (2).

2) Synchronization frame structure and directional synchronization procedure. Now, we explain the directional frame timing synchronization procedure. We start by introducing our employed frame structure, which is shown in Fig. 1. We define a time-slot, which corresponds to one OFDM symbol duration (T_s) . We also define a synchronization frame, in which the BS transmits the downlink synchronization signals to the UEs. As can be seen from Fig. 1, each synchronization frame consists of $T_{\rm BS}$ synchronization time-slots, and the synchronization frames are periodic with $T_{\rm period}$ as the corresponding period. In conventional single-stream beamforming based approaches [11], [19], for a given synchronization time-slot, the BS probes one synchronization beam towards a predefined angular direction using a single RF chain. Across $T_{\rm BS}$ synchronization time-slots, the downlink synchronization beams fully scan the given angular range in a time-division multiplexing (TDM) manner. In Fig. 2 shown at the top of next page, we present a conceptual example to characterize the above described synchronization beam probing procedure, from the perspective of the BS.

Upon awakening from idle mode or power-up, the UE attempts to synchronize to the network and then performs a random access procedure. We therefore define a UE-wise synchronization period here, in which the UE employs fully digital front ends to detect the synchronization signal samples. As can be seen from the right-hand side of Fig. 1, the length of one synchronization period corresponds to the duration of $T_{\rm UE}$ OFDM symbols. Across one synchronization period, the UE correlates the received signal samples with the local reference sequence and computes a peak correlation value. If the peak correlation value is larger than a given threshold, the UE then performs the frame timing synchronization (elaborated later in this section); otherwise, the UE repeats the same procedure

for the next synchronization period for possible timing position detection.

The UE can detect the synchronization signal samples only from the overlap region between the BS-wise synchronization frame and the UE-wise synchronization period. In our model shown in Fig. 1, we assume a full overlap such that the synchronization signal samples sent during a given BS-wise synchronization frame can be fully detected by the UE via its synchronization period. With this assumption, the UE of interest can fully exploit complete synchronization sequences to perform the frame timing synchronization. In practice, however, the full overlap cannot always be guaranteed because the UE's power up process, and therefore the UE-wise synchronization period, is quite random and sporadic. To increase the chance of overlap while at the same time facilitating the timing synchronization process, it may be necessary to (i) increase the duration of the UE-wise synchronization period, and (ii) select an appropriate threshold for peak correlation value comparison. Due to space limits, we omit the detailed discussion regarding the synchronization signal detection as it is not relevant to our proposed method, and depends on specific implementation.

3) Received synchronization signal model. Based on the employed array configurations and synchronization signal structure, we develop the received synchronization signal model assuming $N_{\mathrm{RF}}=1$, i.e., single-stream analog-only beamforming at the BS and $M_{
m RF}=M_{
m tot},$ i.e., fully digital baseband combining at the UE. Note that in Section IV, we will modify the received synchronization signal model by assuming $N_{\rm RF} > 1$. We consider a given UE $u \in \{1, \dots, N_{\rm UE}\}$ in a single cell, where N_{UE} corresponds to the total number of UEs in the cell of interest. For better illustration of the synchronization procedure, we assume $T_{\rm BS}=1$, i.e., a single synchronization time-slot, say, synchronization timeslot 0. Denote the frequency-domain modulated symbol on subcarrier $k = 0, \dots, N-1$ by d[k]. We further assume that all the synchronization signal samples $\{d[0], \dots, d[N-1]\}$ probed during synchronization time-slot 0 are received by the UE across the synchronization period. Based on these assumptions, we now derive the received signal model for our

The symbol vector $\mathbf{d} = [\mathbf{d}[0], \cdots, \mathbf{d}[N-1]]^{\mathrm{T}}$ is first transformed to the time-domain via N-point unitary inverse fast Fourier transforms (IFFTs), generating the discrete-time signals at symbol durations $n = 0, \cdots, N-1$ as

$$d[n] = \frac{1}{\sqrt{N}} \sum_{k=0}^{N-1} d[k] e^{j\frac{2\pi k}{N}n}.$$
 (3)

Before applying an $N_{\rm tot} \times 1$ wideband analog beamforming vector, a cyclic prefix (CP) is added to the symbol vector such that the length of the CP is greater than or equal to the maximum delay spread of the multi-path channels. Each sample in the symbol vector is then transmitted by a common wideband analog beamforming vector f_0 probed from the BS, satisfying the power constraint $[f_0f_0^*]_{a,a} = \frac{1}{N_{\rm tot}}$, where $a = 1, \cdots, N_{\rm tot}$. In this paper, we use superscript (0) to denote variables obtained assuming f_0 .

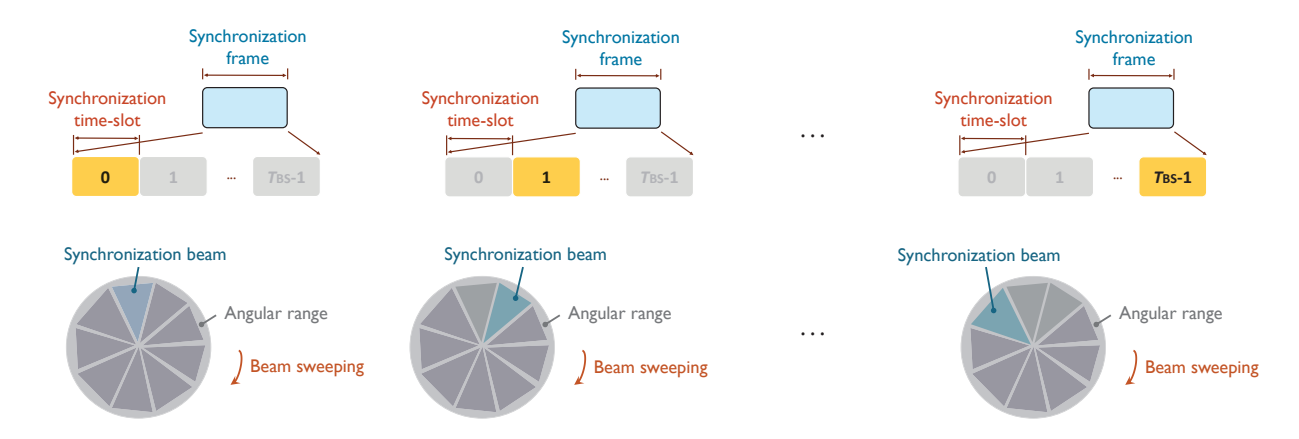


Fig. 2. Across $T_{\rm BS}$ synchronization time-slots, the BS sends the synchronization beams in a TDM manner to cover the given angular space.

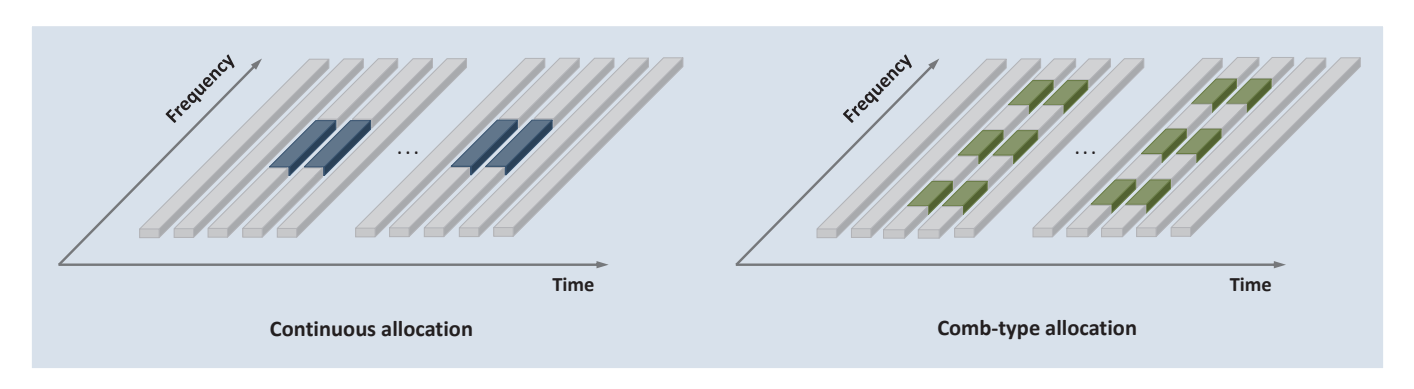


Fig. 3. A conceptual example of continuous and comb-type subcarriers allocation methods for timing synchronization signal. In the continuous allocation strategy, the synchronization signal occupies a set of continuous subcarriers located in the center of the given frequency band. In the comb-type allocation strategy, the synchronization signal is sent across a set of discontinuous and equally spaced sub-signals in the frequency domain.

Considering the b-th receive antenna $(b \in \{1, \cdots, M_{\text{tot}}\})$ at UE u and ignoring the CPs, we denote the time-domain received signal samples by $\mathbf{q}_{u,b}^{(0)} = \left[q_{u,b}^{(0)}[0], \cdots, q_{u,b}^{(0)}[NT_{\text{UE}} - 1]\right]^{\text{T}}$. Denote the number of channel taps by L_u , the corresponding channel impulse response at tap $\ell \in \{0,\cdots,L_u-1\}$ by $\mathbf{H}_u[\ell] \in \mathbb{C}^{M_{\text{tot}} \times N_{\text{tot}}}$, and the additive white Gaussian noise by $w_u[n] \sim \mathcal{N}_{\text{c}}(0,\sigma^2)$. As the UE employs fully digital baseband processing, each receive antenna first quantizes the received synchronization signals with dedicated ADCs. Denote $\mathcal{Q}(\cdot)$ as the quantization function. Further, denote the index of the first synchronization signal sample in the received signal by $\mathbf{t} \in \{0,\cdots,N(T_{\text{UE}}-1)\}$. For $n=0,\cdots,N-1$, the received samples are

$$q_{u,b}^{(0)}[t+n] = \mathcal{Q}\left(\underbrace{\sum_{\ell=0}^{L_u-1} \left[\boldsymbol{H}_u[\ell]\right]_{b,:} \boldsymbol{f}_0 d[((n-\ell))_N] + w_u[n]}_{y_{u,b}^{(0)}[t+n]}\right).$$
(4)

The received signal samples $\{q_{u,b}^{(0)}[0],\cdots,q_{u,b}^{(0)}[NT_{\mathrm{UE}}-1]\}$ also contain non-synchronization signal samples. Hence, we

have

$$q_{u,b}^{(0)}[m'] = \begin{cases} \mathcal{Q}\left(\sum_{\ell=0}^{L_u-1} \left[\boldsymbol{H}_u[\ell]\right]_{b,:} \boldsymbol{f}_0 d[((m'-t-\ell))_N] + w_u[m'-t]\right), m' = t, \cdots, t+N-1, \\ \mathcal{Q}(w_u[m']), \text{ otherwise.} \end{cases}$$
(5)

As can be seen from (5), we model the received non-synchronization signal samples as noise, though they may contain deterministic data and/or control information.

By using the discrete-time received signal vector $\mathbf{q}_{u,b}^{(0)}$ and the known unquantized reference synchronization sequence, the frame timing synchronization can be conducted by UE u. According to (3), the unquantized reference synchronization sequence locally stored at the UE is $\mathbf{d} = [d[0], d[1], \cdots, d[N-1]]^{\mathrm{T}}$. The UE then calculates the time-domain cross-correlation between the received signal samples and the unquantized reference synchronization sequence for the b-th receive antenna as

$$\Gamma_{u,b}^{(0)}[\nu] = \sum_{n=0}^{N-1} q_{u,b}^{(0)}[n+\nu]d^*[n], \tag{6}$$

where $\nu=0,\cdots,N(T_{\rm UE}-1)$. Denote the index of the selected receive antenna by \hat{b} . The maximum likelihood detector

[21] finds $\hat{\nu}$ that corresponds to the peak in the correlation, i.e.,

$$\left(\hat{\nu}, \hat{b}\right) = \underset{\substack{\nu = 0, \dots, N(T_{\text{UE}} - 1)\\b = 1, \dots, M_{\text{ext}}}}{\operatorname{argmax}} \left| \Gamma_{u,b}^{(0)}[\nu] \right|^2. \tag{7}$$

If $\left|\Gamma_{u,\hat{b}}^{(0)}[\hat{\nu}]\right|^2$ is larger than a given threshold, say $\tau_{\rm corr}$, UE u determines $\hat{\nu}$ as the estimate of the frame timing position. Otherwise, the UE repeats the above procedure until the correlation peak is above the threshold. If $\mathcal{Q}(\cdot)$ in (4) and (5) corresponds to low-resolution quantization (e.g., 1-4 bits), the corresponding quantization distortion will damage the good correlation properties of the employed synchronization sequences, leading to degraded timing synchronization performance.

4) Resource allocation for synchronization signal. In this paper, we consider two subcarrier and synchronization signal mapping strategies, which are (i) continuous subcarriers allocation, and (ii) comb-type subcarriers allocation. In Fig. 3, we depict a conceptual example to characterize these two design options. As can be seen from Fig. 3, in the continuous subcarriers allocation strategy, we map the synchronization sequence onto a set of continuous subcarriers in the frequency domain, symmetrically surrounding the direct current (DC)carrier. This mapping strategy is similar to the primary synchronization signal (PSS) structure in LTE systems, where the ZC sequence is mapped onto the central $N_{\rm ZC}$ subcarriers out of N subcarriers surrounding the DC-carrier symmetrically. Note that for the continuous subcarriers allocation in this paper, we set the DC-carrier as zero as in LTE systems [9]; it is worth noting that no explicit DC-carrier is reserved for both the downlink and uplink in the 3GPP 5G NR systems (Release 15) [11]. In the comb-type subcarriers allocation method, we also assign a set of continuous subcarriers to a synchronization sequence (i.e., a sub-signal), but send multiple such subsignals (N_{sub}) in a given synchronization time-slot (as shown in Fig. 3). In the case of the ZC sequence design, each subsignal corresponds to a complete length- $N_{\rm ZC}$ ZC sequence. Multiple identical ZC sequences with the same root index (corresponding to multiple sub-signals) are then transmitted during a given synchronization time-slot. Different from the continuous allocation strategy, the DC-carrier is not reserved for the comb-type resource mapping design. The comb-type PSS structure was originally proposed in [13] for cell discovery in mmWave systems. In this paper, we use this design for low-resolution timing synchronization. By configuring a minimum possible bandwidth for each sub-signal, the combtype design can better enforce the flat channel and constant quantization distortion assumptions, which will be elaborated in Section III-A. Further, by exploiting frequency diversity of mmWave channels via the comb-type structure, good timing synchronization performance can be achieved. For simplicity, we employ the continuous subcarriers allocation strategy to illustrate the problem formulation, design principle, and implementation procedure of our proposed solution. Note that they can be extended to the comb-type assignment with moderate modifications. In Section V, we numerically compare the

comb-type and continuous subcarriers allocation strategies in terms of the timing position estimation performance.

B. Channel model

Assume that the channel between the BS and UE $u \in \{1,\cdots,N_{\mathrm{UE}}\}$ has R_u paths, and each path r has azimuth and elevation angle-of-departures (AoDs) $\phi_{u,r},\theta_{u,r}$ and angle-of-arrival (AoA) $\psi_{u,r}$. Let $p(\tau)$ denote the combined effect of filtering and pulse shaping for T_{s} -spaced signaling at τ seconds. We then express the time-domain delay- ℓ MIMO channel matrix as

$$\boldsymbol{H}_{u}[\ell] = \sum_{r=1}^{R_{u}} \beta_{u,r} p\left(\ell T_{s} - \tau_{r}\right) \boldsymbol{a}_{rx}(\psi_{u,r}) \boldsymbol{a}_{tx}^{*}(\theta_{u,r}, \phi_{u,r}), \quad (8)$$

where $\beta_{u,r}$ represents the complex path gain of path-r between the BS and UE u, and $a_{\rm rx}(\cdot) \in \mathbb{C}^{M_{\rm tot} \times 1}$ and $a_{\rm tx}(\cdot, \cdot) \in \mathbb{C}^{N_{\rm tot} \times 1}$ and $a_{\rm tx}(\cdot, \cdot) \in \mathbb{C}^{N_{\rm tot} \times 1}$ correspond to the receive and transmit array response vectors. For instance, if the BS employs a uniform planar array (UPA) in the xy-plane and the UE uses a uniform linear array (ULA) on the y axis, $a_{\rm tx}(\cdot, \cdot)$ and $a_{\rm rx}(\cdot)$ would exhibit the same structures as those in (3) and (4) in [22]. By taking the Fourier transform of $H_u[\ell]$, we can obtain the corresponding frequency-domain channel matrix $\mathbf{H}_u[k]$ for $k=0,\cdots,N-1$. In Sections III and IV, we use $H_u[\ell]$ to develop the received synchronization signal model in the time-domain and $\mathbf{H}_u[k]$ to illustrate the proposed algorithm in the frequency-domain.

III. PROBLEM FORMULATION AND DESIGN INSIGHTS

In this section, we first formulate the directional frame timing synchronization problem for mmWave systems operating with low-resolution ADCs. We then show that the formulated problem is a max-min multicast optimization problem, which cannot be effectively solved under the framework of single-stream beamforming. For clarity, we conduct the problem formulation using the frequency-domain representations, though we first present the received signal model in the time-domain.

A. Received synchronization SQNR formulation

To formulate the optimization problem for low-resolution timing synchronization, we need to first determine a proper optimization metric. Similar to Section II-A, we assume a single synchronization time-slot, single-stream analog-only beamforming at the BS and fully digital baseband processing at the UE. By Bussgang's theorem [17], [18] and assuming independent and identically distributed (IID) Gaussian input to the quantizer, the quantization output in (4) can be decoupled into a signal part and an uncorrelated distortion component. We first define $\boldsymbol{E}_{u,b}^{(0)} = \operatorname{diag}\left(\left[\eta_{u,b}^{(0)}[0],\cdots,\eta_{u,b}^{(0)}[N-1]\right]^{\mathrm{T}}\right)$ as the quantization distortion matrix with

$$\eta_{u,b}^{(0)}[n] = \frac{\mathbb{E}\left[\left(q_{u,b}^{(0)}[t+n]\right)^* y_{u,b}^{(0)}[t+n]\right]}{\mathbb{E}\left[\left|y_{u,b}^{(0)}[t+n]\right|^2\right]},\tag{9}$$

as the distortion factor of the quantization, which depends on the quantizer design, the number of quantization bits and

$$\gamma_{u,\hat{b}}^{(0)} = \frac{\underline{\eta}_{u,\hat{b}}^{(0)} \mathbf{g}_{u}^{2} \left| [\mathbf{a}_{\text{rx}}(\psi_{u}) \mathbf{a}_{\text{tx}}^{*}(\theta_{u}, \phi_{u})]_{\hat{b},:} \mathbf{f}_{0} \right|^{2}}{\underline{\eta}_{u,\hat{b}}^{(0)} \sigma^{2} + \left(1 - \underline{\eta}_{u,\hat{b}}^{(0)}\right) \left(\mathbf{g}_{u}^{2} \left| [\mathbf{a}_{\text{rx}}(\psi_{u}) \mathbf{a}_{\text{tx}}^{*}(\theta_{u}, \phi_{u})]_{\hat{b},:} \mathbf{f}_{0} \right|^{2} + \sigma^{2}\right)}.$$
(19)

the distribution of the input samples to the quantizer [23]. Rewriting

$$\mathbf{d}_{\ell} = \left[d[((-\ell))_{N}], d[((1-\ell))_{N}], \cdots, d[((N-1-\ell))_{N}] \right]^{\mathrm{T}},$$
 (10)

and $q_{u,b}^{(0)} = \left[q_{u,b}^{(0)}[\mathbf{t}], \cdots, q_{u,b}^{(0)}[\mathbf{t}+N-1]\right]^{\mathrm{T}}$, we then decompose (4) as

$$\boldsymbol{q}_{u,b}^{(0)} = \boldsymbol{E}_{u,b}^{(0)} \left(\underbrace{\sum_{\ell=0}^{L_u-1} \left[\boldsymbol{H}_u[\ell] \right]_{b,:} \boldsymbol{f}_0 \boldsymbol{d}_{\ell}}_{\boldsymbol{v}_{u,b}^{(0)}} + \boldsymbol{w}_u \right) + \check{\boldsymbol{w}}_{u,b}^{(0)}. \tag{11}$$

Denote the quantization mean squared error by ξ_u assuming Gaussian signaling with unit variance [24]. We further denote the covariance matrix of the noiseless unquantized received signal $v_{u,b}^{(0)}$ in (11) by $R_{v_{u,b}^{(0)}}$ and the additive quantization noise

vector by $\check{\boldsymbol{w}}_{u,b}^{(0)} = \left[\check{\boldsymbol{w}}_{u,b}^{(0)}[0], \cdots, \check{\boldsymbol{w}}_{u,b}^{(0)}[N-1]\right]^{\mathrm{T}}$. As shown in [24], the quantization distortion matrix $\boldsymbol{E}_{u,b}^{(0)}$ can then be computed as

$$\boldsymbol{E}_{u,b}^{(0)} = (1 - \xi_u) \operatorname{diag} \left(\boldsymbol{R}_{\boldsymbol{v}_{u,b}^{(0)}} + \sigma^2 \boldsymbol{I}_N \right)^{-\frac{1}{2}}.$$
 (12)

Denoting the unquantized received signal power matrix for the *b*-th receive antenna at UE u by $V_{u,b}^{(0)}$, we can express the covariance matrix of the quantization noise vector $\check{\boldsymbol{w}}_{u,b}^{(0)}$ as [24], [25]

$$\mathbf{R}_{\check{w}_{u,b}^{(0)}} = \mathbf{E}_{u,b}^{(0)} \left(\mathbf{I}_{N} - \mathbf{E}_{u,b}^{(0)} \right) \underbrace{\operatorname{diag} \left(\mathbf{R}_{v_{u,b}^{(0)}} + \sigma^{2} \mathbf{I}_{N} \right)}_{\mathbf{V}_{u,b}^{(0)}}.$$
 (13)

As can be seen from (12) and (13), both $E_{u,b}^{(0)}$ and $R_{\check{w}_{u,b}^{(0)}}$, depend on $R_{v_{u,b}^{(0)}}$, which depends on the effective beam-space channel.

In the following, we compute the zero-lag correlation between the received signal samples and the known unquantized reference synchronization sequence in the frequency-domain. We first express the frequency-domain quantized received signal $\mathbf{q}_{u,b}^{(0)} = \left[\mathbf{q}_{u,b}^{(0)}[0],\cdots,\mathbf{q}_{u,b}^{(0)}[N-1]\right]^{\mathrm{T}}$ as

$$\mathbf{q}_{u,b}^{(0)}[k] = \eta_{u,b}^{(0)}[k] \left[\mathbf{H}_{u}[k] \right]_{b,:} \mathbf{f}_{0} \mathbf{d}[k] + \eta_{u,b}^{(0)}[k] \mathbf{w}_{u}[k] + \check{\mathbf{w}}_{u,b}^{(0)}[k],$$
(14)

where $\check{\mathbf{w}}_{u,b}^{(0)}[k] = \sum_{n=0}^{N-1} \check{w}_{u,b}^{(0)}[n] e^{-\mathrm{j}2\pi nk/N}$. We then calculate the zero-lag frequency-domain correlation between $\mathbf{q}_{u,b}^{(0)}$ and the unquantized reference synchronization sequence \mathbf{d} as

$$\Lambda_{u,b}^{(0)}[0] = \sum_{k=0}^{N-1} \mathsf{q}_{u,b}^{(0)}[k] \mathsf{d}^*[k]$$
 (15)

$$= \sum_{k=0}^{N-1} \eta_{u,b}^{(0)}[k] \left[\mathbf{H}_{u}[k] \right]_{b,:} \mathbf{f}_{0} \mathsf{d}[k] \mathsf{d}^{*}[k]$$

$$+ \sum_{k=0}^{N-1} \eta_{u,b}^{(0)}[k] \mathbf{w}_{u}[k] \mathsf{d}^{*}[k] + \sum_{k=0}^{N-1} \check{\mathbf{w}}_{u,b}^{(0)}[k] \mathsf{d}^{*}[k].$$

$$(16)$$

Similar to (6), we have $\hat{b} = \underset{b=1,\cdots,M_{\mathrm{tot}}}{\operatorname{argmax}} \left| \Lambda_{u,b}^{(0)}[0] \right|^2$. Different from high-rate data communications, the synchronization signals usually occupy a relatively small portion of the entire bandwidth with continuous subcarriers surrounding the DCcarrier. For instance, in LTE systems [9], the synchronization signal samples occupy 62 subcarriers (out of 1024 for 10 MHz bandwidth, or 2048 for 20 MHz bandwidth) surrounding the DC-carrier. If the same design principle applies to mmWave systems, along with the sparse nature of the mmWave channels, the synchronization signals will most likely experience "flat" channels instead of severe frequency selectivity. It is also worth noting that the ZC-type sequences are robust to the frequency selectivity [26]. If the channels significantly fluctuate across the occupied subcarriers, the flat channel assumption for synchronization may no longer hold. In this case, it is essential to optimize the sequence length to fit for the minimum possible bandwidth. Leveraging the flat channel assumption for synchronization and denoting the frequencydomain counterpart of the unquantized received signal power matrix $V_{\alpha,\hat{b}}^{(0)}$ in (13) by $V_{\alpha,\hat{b}}^{(0)}$, we can first obtain

$$\mathbf{V}_{u,\hat{b}}^{(0)} = \mathbf{g}_{u}^{2} \left| \left[\mathbf{a}_{\text{rx}}(\psi_{u}) \mathbf{a}_{\text{tx}}^{*}(\theta_{u}, \phi_{u}) \right]_{\hat{b},:} \mathbf{f}_{0} \right|^{2} \operatorname{diag}\left(\mathbf{dd}^{*}\right) + \sigma^{2} \mathbf{I}_{N}$$

$$= \mathbf{g}_{u}^{2} \left| \left[\mathbf{a}_{\text{rx}}(\psi_{u}) \mathbf{a}_{\text{tx}}^{*}(\theta_{u}, \phi_{u}) \right]_{\hat{b},:} \mathbf{f}_{0} \right|^{2}$$

$$\times \operatorname{diag}\left(\left[\mathbf{d}[0] \mathbf{d}^{*}[0], \cdots, \mathbf{d}[N-1] \mathbf{d}^{*}[N-1] \right]^{T} \right)$$

$$+ \sigma^{2} \mathbf{I}_{N},$$

$$(18)$$

where g_u^2 is the frequency-domain channel gain without path and subcarrier indices. Also because of the flat channel assumption, we define $\underline{\eta}_{u,\hat{b}}^{(0)} = \eta_{u,\hat{b}}^{(0)}[0] = \cdots = \eta_{u,\hat{b}}^{(0)}[N-1]$ as a common quantization distortion factor. By exploiting the inherent correlation properties of the ZC sequence design in (2), we can compute the quantization noise power using (12), (13) and (18). We can then formulate the corresponding received synchronization SQNR at zero-lag correlation for UE u in (19), which is shown at the top of this page.

Similar to the calculation of $\Lambda_{u,b}^{(0)}[0]$ in (15), we can also compute the non-zero-lag correlation values. In Fig. 4, we plot the absolute correlation values of the employed synchronization sequence under both infinite-resolution and 2-bit ADCs. Both zero-lag and non-zero-lag correlations are

$$\gamma_{u,\hat{b}}^{(0)} = \frac{\underline{\eta}_{u,\hat{b}}^{(0)} \left| \boldsymbol{a}_{\text{tx}}^{*}(\theta_{u}, \phi_{u}) \boldsymbol{f}_{0} \right|^{2}}{\underline{\eta}_{u,\hat{b}}^{(0)} \underline{g}_{u}^{2} \left| \left[\boldsymbol{a}_{\text{rx}}(\psi_{u}) \right]_{\hat{b}} \right|^{2} + \left(1 - \underline{\eta}_{u,\hat{b}}^{(0)} \right) \left(\left| \boldsymbol{a}_{\text{tx}}^{*}(\theta_{u}, \phi_{u}) \boldsymbol{f}_{0} \right|^{2} + \underline{g}_{u}^{2} \left| \left[\boldsymbol{a}_{\text{rx}}(\psi_{u}) \right]_{\hat{b}} \right|^{2}} \right)}$$
(23)

$$= \frac{\underline{\eta}_{u,\hat{b}}^{(0)} \left| \boldsymbol{a}_{tx}^{*}(\theta_{u}, \phi_{u}) \boldsymbol{f}_{0} \right|^{2}}{\underline{\eta}_{u,\hat{b}}^{(0)} \lambda_{u} + \left(1 - \underline{\eta}_{u,\hat{b}}^{(0)} \right) \left(\left| \boldsymbol{a}_{tx}^{*}(\theta_{u}, \phi_{u}) \boldsymbol{f}_{0} \right|^{2} + \lambda_{u} \right)}.$$
(24)

$$\dot{\gamma}_{u}^{(0)} = \frac{\left|\boldsymbol{a}_{\text{tx}}^{*}(\theta_{u}, \phi_{u})\boldsymbol{f}_{0}\right|^{2}}{\lambda_{\text{max}} + \left[\frac{\left[\sigma^{2}\left(\left|\boldsymbol{a}_{\text{tx}}^{*}(\theta_{u}, \phi_{u})\boldsymbol{f}_{0}\right|^{2}/\lambda_{\text{max}}+1\right)\right]^{1/2}}{1-\xi_{u}} - 1\right]\left(\left|\boldsymbol{a}_{\text{tx}}^{*}(\theta_{u}, \phi_{u})\boldsymbol{f}_{0}\right|^{2} + \lambda_{\text{max}}\right)},$$
(27)

$$\dot{\gamma}_{u}^{(0)} = \frac{|\boldsymbol{a}_{\text{tx}}^{*}(\boldsymbol{\theta}_{u}, \boldsymbol{\phi}_{u})\boldsymbol{f}_{0}|^{2}}{\lambda_{\text{max}} + \left[\frac{\left[\sigma^{2}\left(|\boldsymbol{a}_{\text{tx}}^{*}(\boldsymbol{\theta}_{u}, \boldsymbol{\phi}_{u})\boldsymbol{f}_{0}|^{2}/\lambda_{\text{max}}+1\right)\right]^{1/2}}{1-\xi_{\text{max}}} - 1\right]\left(|\boldsymbol{a}_{\text{tx}}^{*}(\boldsymbol{\theta}_{u}, \boldsymbol{\phi}_{u})\boldsymbol{f}_{0}|^{2} + \lambda_{\text{max}}\right)}.$$
(28)

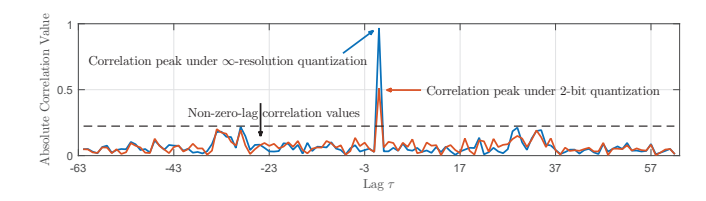


Fig. 4. Absolute correlation values of the employed synchronization sequence under both infinite-resolution and 2-bit ADCs. A length-62 ZC sequence with root index 34 is used.

revealed in this example. As can be seen from Fig. 4, for both infinite-resolution and 2-bit ADCs, the non-zero-lag correlation values have small magnitudes and exhibit similar patterns. For the zero-lag correlation, however, the correlation peak obtained under 2-bit ADCs is much smaller than that under ∞-resolution quantization. Leveraging these observations, we employ the received synchronization SQNR at zero-lag correlation as the main optimization metric and formulate the corresponding optimization problems in Section III-B.

B. Single-stream multicast beamforming

We first consider a single UE, e.g., UE u and a single synchronization time-slot, e.g., synchronization time-slot 0. Our design target here is to maximize the received synchronization SQNR at zero-lag correlation for UE u. Note that in (19), the only parameter that can be tuned is the beamforming vector. To better compensate for the quantization distortion, it is therefore desirable to custom design the synchronization beams as long as necessary information is available at the BS. This is different from traditional TDM probing based approaches [11], [19], where the synchronization beams are predetermined and fixed. According to (19), we can formulate this maximization problem as

$$\mathcal{P}0: \max_{\boldsymbol{f}_0} \left\{ \gamma_{u,\hat{b}}^{(0)} \right\} \tag{20}$$

s.t.
$$[f_0f_0^*]_{a,a} = \frac{1}{N_{\text{tot}}}, a = 1, \dots, N_{\text{tot}}.$$

To simplify $\mathcal{P}0$, we assume that the BS uses a predefined analog beam codebook \mathcal{F} , having a limited number of beam codewords. We can then reformulate (20) as

$$\mathcal{P}1: \max_{f_0} \left\{ \gamma_{u,\hat{b}}^{(0)} \right\}$$
s.t. $f_0 \in \mathcal{F}$.

Solving $\mathcal{P}1$ does not increase the non-zero-lag correlation values at the same pace as the zero-lag peak correlation value. That is, by maximizing the received synchronization SQNR at zero-lag correlation, the power difference between the zero-lag peak correlation value and the non-zero-lag correlation values assuming low-resolution quantization is also maximized.

Next, we extend the problem formulation to a single cell with multiple UEs. In this case, we expect that for a given synchronization time-slot, a group of UEs can simultaneously synchronize to the network with satisfying synchronization performance. This reduces the overall access delay of the network. The design target therefore becomes maximizing the minimum received synchronization SQNR at zero-lag correlation for all potential UEs. Assuming a total of $N_{\rm UE}$ UEs and synchronization time-slot 0, we formulate the following max-min optimization problem as

$$\mathcal{P}2: \max_{\mathbf{f}_0} \min_{\forall u} \left\{ \gamma_{u,\hat{b}}^{(0)} \right\}$$
s.t. $\mathbf{f}_0 \in \mathcal{F}$. (22)

Denoting by $\lambda_u = \sigma^2/\mathsf{g}_u^2 \left| [a_{\rm rx}(\psi_u)]_{\hat{b}} \right|^2$, we rewrite $\gamma_{u,\hat{b}}^{(0)}$ in (24), shown at the top of this page. We can interpret λ_u as the inverse of the received SNR at UE u. Denoting by $\lambda_{\rm max} = \max\{\lambda_1,\cdots,\lambda_{N_{\rm UE}}\}$ and replacing λ_u in (24) with $\lambda_{\rm max}$, we define a lower bound of $\gamma_{u,\hat{b}}^{(0)}$ as

$$\tilde{\gamma}_{u,\hat{b}}^{(0)} = \frac{\underline{\eta}_{u,\hat{b}}^{(0)} |\boldsymbol{a}_{tx}^*(\theta_u, \phi_u) \boldsymbol{f}_0|^2}{\underline{\eta}_{u,\hat{b}}^{(0)} \lambda_{\max} + \left(1 - \underline{\eta}_{u,\hat{b}}^{(0)}\right) \left(|\boldsymbol{a}_{tx}^*(\theta_u, \phi_u) \boldsymbol{f}_0|^2 + \lambda_{\max}\right)}.$$
(25)

For any given UE u, we therefore have

$$\check{\gamma}_{u,\hat{b}}^{(0)} \le \gamma_{u,\hat{b}}^{(0)}.$$
(26)

By plugging the results of (12) and (18) into (25), we obtain (27) (at the top of the previous page), which becomes irrelevant to the selected receive antenna index \hat{b} for UE u. Denoting by $\xi_{\max} = \max\{\xi_1, \cdots, \xi_{N_{\mathrm{UE}}}\}$ and replacing ξ_u in (27) with ξ_{\max} , we can further define a lower bound of $\check{\gamma}_u^{(0)}$ in (28), which is also shown at the top of the previous page. That is, for any given UE u, we have

$$\dot{\gamma}_{u}^{(0)} \le \ddot{\gamma}_{u}^{(0)}.\tag{29}$$

Note that $1/\lambda_{\rm max}$ and $1-\xi_{\rm max}$ represent the lowest received SNR and the quantization distortion factor corresponding to the lowest-resolution ADC among all UEs, and they can be used to characterize the worst-case scenario of the network. Based on (26) and (29), we can therefore reformulate the optimization problem in (22) as

$$\mathcal{P}3: \max_{f_0} \min_{\forall u} \left\{ \dot{\gamma}_u^{(0)} \right\}$$
s.t. $f_0 \in \mathcal{F}$. (30)

Solving (30) requires explicit knowledge of θ_u 's, ϕ_u 's, λ_u 's ($\lambda_{\rm max}$), and ξ_u 's ($\xi_{\rm max}$) for all UEs ($u=1,\cdots,N_{\rm UE}$). In practice, $\lambda_{\rm max}$ and $\xi_{\rm max}$ can be replaced with predefined system specific parameters that best characterize the network condition. The explicit channel directional information, however, is unavailable during the initial timing synchronization phase.

In addition, the limited beam codebook resolution limits the design degrees of freedom for the single-stream multicast beamforming to solve the low-resolution timing synchronization problem. Prior to explicitly explaining this issue, we first define two terminologies, which are low-resolution waveform and high-resolution waveform. In this paper, we refer to the case with limited phase shifters resolution (characterized by \mathcal{F}) as the low-resolution waveform, and the case with highresolution phase shifters as the high-resolution waveform. Under ∞-bit ADCs, both the high-resolution waveform and lowresolution waveform can provide good received signal quality. Under few-bit ADCs, however, only the high-resolution waveform can work well because its higher resolution can compensate for the additional ADC quantization loss. Using the high-resolution waveform may not be practical because: (i) high-resolution phase shifters have higher hardware cost and power consumption, and (ii) non-uniform phase shifters quantization may be required in our case, which may result in even higher implementation costs. Our design target therefore becomes to synthesize the high-resolution waveform from the low-cost low-resolution waveforms to improve the timing synchronization performance under few-bit ADCs. In Section IV, we explicitly discuss our proposed multi-beam probing based strategy with common synchronization signal design to achieve this objective.

IV. PROPOSED MULTI-BEAM PROBING BASED SYNCHRONIZATION METHOD

In this section, we develop a new multi-beam probing based low-resolution timing synchronization strategy to effectively solve the multicast problem. Along with a common synchronization signal structure design, the proposed method exploits the spatial degrees of freedom arising from multiple RF chains to compensate for the quantization distortion without requiring explicit channel knowledge. Similar to Section III, we explain the proposed algorithm using the frequency-domain representations, though we first present the received signal model in the time-domain.

A. Received signal model for multi-beam probing

We assume that for a given synchronization time-slot, the BS deploys multiple subarrays to simultaneously form multiple analog synchronization beams, through which a total of $N_{\rm UE}$ UEs synchronize to the network. This is different from the conventional directional synchronization design in Section III-A, in which the BS probes one beam at a time. Further, for the given synchronization time-slot, we assume that the BS transmits common synchronization signals (or identical synchronization sequences) across the simultaneously probed beams. This is also different from conventional MIMO communications, in which distinct signals are spatially multiplexed to boost the capacity.

For a given synchronization time-slot, we denote the employed analog precoding matrix at the BS as

$$P = \begin{bmatrix} p_0 & \mathbf{0}_{N_{\text{A}} \times 1} & \cdots & \mathbf{0}_{N_{\text{A}} \times 1} \\ \mathbf{0}_{N_{\text{A}} \times 1} & p_1 & \cdots & \mathbf{0}_{N_{\text{A}} \times 1} \\ \vdots & \vdots & \ddots & \vdots \\ \mathbf{0}_{N_{\text{A}} \times 1} & \mathbf{0}_{N_{\text{A}} \times 1} & \cdots & p_{N_{\text{RF}} - 1} \end{bmatrix}, \quad (31)$$

where for $j=0,\cdots,N_{\rm RF}-1$, the beam probed from the j-th transmit RF chain $\boldsymbol{p}_j\in\mathbb{C}^{N_{\rm A}\times 1}$ satisfies the power constraint $\left[\boldsymbol{p}_j\boldsymbol{p}_j^*\right]_{a,a}=\frac{1}{N_{\rm A}}$ with $a=1,\cdots,N_{\rm A}.$ Denote the set of the analog synchronization beams by $\Omega=\{\boldsymbol{p}_0,\cdots,\boldsymbol{p}_{N_{\rm RF}-1}\}.$ Similar to (4), we can then express the quantized timedomain received signal on the b-th receive antenna at UE $u\in\{1,\cdots,N_{\rm UE}\}$ as

$$q_{u,b}^{\Omega}[\mathbf{t}+n] = \mathcal{Q}\left(y_{u,b}^{\Omega}[\mathbf{t}+n]\right)$$
(32)
$$= \mathcal{Q}\left(\left[\sum_{\ell=0}^{L_{u}-1} \sqrt{\frac{1}{N_{RF}}} \mathbf{H}_{u}[\ell] \mathbf{P}\left(d[((k-\ell))_{N}] \mathbf{1}_{N_{RF} \times 1}\right)\right]_{b}$$

$$+ w_{u}[n]\right)$$
(33)
$$= \mathcal{Q}\left(\sum_{\ell=0}^{L_{u}-1} \sum_{j=0}^{N_{RF}-1} \sqrt{\frac{1}{N_{RF}}} \left(\left[\mathbf{H}_{u}[\ell]\right]_{b,jN_{A}+1:(j+1)N_{A}} \mathbf{p}_{j}\right)$$

$$\times d[((n-\ell))_{N}] + w_{u}[n]\right),$$
(34)

where the transmit power is scaled by the number of streams, i.e., $N_{\rm RF}$, to maintain the total power constraint. Note that

 $\mathbf{1}_{N_{\mathrm{RF}} imes 1}$ in (33) indicates the common synchronization signal structure

To express (34) in vector form, we first denote $h_{u,b}^{\Omega}[\ell] = \sum_{j=0}^{N_{\mathrm{RF}}-1} [\boldsymbol{H}_{u}[\ell]]_{b,jN_{\mathrm{A}}+1:(j+1)N_{\mathrm{A}}} \boldsymbol{p}_{j}$ as the time-domain composite effective transmit beam-space channel and $\boldsymbol{q}_{u,b}^{\Omega} = \left[q_{u,b}^{\Omega}[t], \cdots, q_{u,b}^{\Omega}[t+N-1]\right]^{\mathrm{T}}$. By applying Bussgang's theorem, we then have

$$\boldsymbol{q}_{u,b}^{\Omega} = \boldsymbol{E}_{u,b}^{\Omega} \left(\underbrace{\sum_{\ell=0}^{L_u-1} \sqrt{\frac{1}{N_{\mathrm{RF}}}} h_{u,b}^{\Omega}[\ell] \boldsymbol{d}_{\ell}}_{\boldsymbol{v}_{u,b}^{\Omega}} + \boldsymbol{w}_{u} + \check{\boldsymbol{w}}_{u,b}^{\Omega}, \quad (35)$$

where the quantization distortion matrix $\boldsymbol{E}_{u,b}^{\Omega} = \operatorname{diag}\left(\left[\eta_{u,b}^{\Omega}[0],\cdots,\eta_{u,b}^{\Omega}[N-1]\right]^{\mathrm{T}}\right)$, and similar to (9), the corresponding quantization distortion factor is

$$\eta_{u,b}^{\Omega}[n] = \frac{\mathbb{E}\left[(q_{u,b}^{\Omega}[t+n])^* y_{u,b}^{\Omega}[t+n] \right]}{\mathbb{E}\left[\left| y_{u,b}^{\Omega}[t+n] \right|^2 \right]}.$$
 (36)

Denoting the covariance matrix of the noiseless unquantized received signal $v_{u,b}^{\Omega}$ in (35) by $R_{v_{u,b}^{\Omega}}$, we can further express $E_{u,b}^{\Omega}$ as

$$\boldsymbol{E}_{u,b}^{\Omega} = (1 - \xi_u) \operatorname{diag} \left(\boldsymbol{R}_{\boldsymbol{v}_{u,b}^{\Omega}} + \sigma^2 \boldsymbol{I}_N \right)^{-\frac{1}{2}}.$$
 (37)

The covariance matrix of the quantization noise vector $\check{\boldsymbol{w}}_{u,b}^{\Omega}$ with respect to the *b*-th receive antenna at UE *u* now becomes

$$\boldsymbol{R}_{\boldsymbol{\dot{w}}_{u,b}^{\Omega}} = \boldsymbol{E}_{u,b}^{\Omega} \left(\boldsymbol{I}_{N} - \boldsymbol{E}_{u,b}^{\Omega} \right) \underbrace{\operatorname{diag} \left(\boldsymbol{R}_{\boldsymbol{v}_{u,b}^{\Omega}} + \sigma^{2} \boldsymbol{I}_{N} \right)}_{\boldsymbol{V}_{u,b}^{\Omega}}, \quad (38)$$

where $V_{u,b}^{\Omega}$ represents the corresponding unquantized received signal power matrix.

B. Optimization problem formulation for multi-beam probing

Prior to formulating the low-resolution timing synchronization problem for the proposed multi-beam probing, we need to first derive the correlation between the frequency-domain quantized received synchronization signal $\mathbf{q}_{u,b}^{\Omega}$ and the known unquantized reference synchronization sequence \mathbf{d} . Denoting

$$\mathbf{h}_{u,b}^{\Omega}[k] = \sum_{j=0}^{N_{\text{RF}}-1} \left[\mathbf{H}_{u}[k] \right]_{b,jN_{\text{A}}+1:(j+1)N_{\text{A}}} \boldsymbol{p}_{j}, \quad (39)$$

as the frequency-domain composite effective transmit beamspace channel relative to its time-domain counterpart $h_{u,b}^{\Omega}[\ell]$, we can compute the zero-lag frequency-domain correlation for UE u as

$$\begin{split} &\Lambda_{u,b}^{\Omega}[0] = \sum_{k=0}^{N-1} \mathsf{q}_{u,b}^{\Omega}[k] \mathsf{d}^{*}[k] \\ &= \sum_{k=0}^{N-1} \eta_{u,b}^{\Omega}[k] \sqrt{\frac{1}{N_{\mathrm{RF}}}} \mathsf{h}_{u,b}^{\Omega}[k] \mathsf{d}[k] \mathsf{d}^{*}[k] \\ &+ \sum_{k=0}^{N-1} \eta_{u,b}^{\Omega}[k] \mathsf{w}_{u}[k] \mathsf{d}^{*}[k] + \sum_{k=0}^{N-1} \check{\mathsf{w}}_{u,b}^{\Omega}[k] \mathsf{d}^{*}[k]. \end{split} \tag{40}$$

Denoting by $\hat{b} = \underset{b=1,\cdots,M_{\mathrm{tot}}}{\operatorname{argmax}} \left| \Lambda_{u,b}^{\Omega}[0] \right|^2$ and applying the same flat channel assumption for synchronization as in (19), we can rewrite the frequency-domain composite effective transmit beam-space channel in (39) as

$$\mathbf{h}_{u}^{\Omega} = \sum_{j=0}^{N_{\mathrm{RF}}-1} \left[\boldsymbol{a}_{\mathrm{tx}}^{*}(\theta_{u}, \phi_{u}) \right]_{jN_{\mathrm{A}}+1:(j+1)N_{\mathrm{A}}} \boldsymbol{p}_{j}. \tag{42}$$

Further, denoting the frequency-domain counterpart of the unquantized received signal power matrix $V_{u,\hat{b}}^{\Omega}$ in (38) by $\mathbf{V}_{u,\hat{b}}^{\Omega}$, we have

$$\mathbf{V}_{u,\hat{b}}^{\Omega} = \frac{\mathbf{g}_{u}^{2} \left| \left[\mathbf{a}_{rx}(\psi_{u}) \right]_{\hat{b}} \right|^{2}}{N_{RF}} \left| \mathbf{h}_{u}^{\Omega} \right|^{2} \times \operatorname{diag} \left(\left[\mathsf{d}[0] \mathsf{d}^{*}[0], \cdots, \mathsf{d}[N-1] \mathsf{d}^{*}[N-1] \right]^{T} \right) + \sigma^{2} \mathbf{I}_{N}.$$

$$(43)$$

By exploiting the inherent correlation properties of the common synchronization signal design and applying the common quantization distortion factor $\underline{\eta}_{u,\hat{b}}^{\Omega} = \eta_{u,\hat{b}}^{\Omega}[0] = \cdots = \eta_{u,\hat{b}}^{\Omega}[N-1]$, we can obtain the quantization noise power by using (37), (38) and (43), which results in the received synchronization SQNR at zero-lag correlation for UE u as

$$\gamma_{u,\hat{b}}^{\Omega} = \frac{\underline{\eta_{u,\hat{b}}^{\Omega}} \frac{\mathbf{g}_{u}^{2} \left| \left[\mathbf{a}_{\text{rx}}(\psi_{u}) \right]_{\hat{b}} \right|^{2}}{N_{\text{RF}}} \left| \mathbf{h}_{u}^{\Omega} \right|^{2}}{\underline{\eta_{u,\hat{b}}^{\Omega}} \sigma^{2} + \left(1 - \underline{\eta}_{u,\hat{b}}^{\Omega} \right) \left(\frac{\mathbf{g}_{u}^{2} \left| \left[\mathbf{a}_{\text{rx}}(\psi_{u}) \right]_{\hat{b}} \right|^{2}}{N_{\text{RF}}} \left| \mathbf{h}_{u}^{\Omega} \right|^{2} + \sigma^{2} \right)}. \tag{44}$$

For the given synchronization time-slot, we formulate the corresponding max-min optimization problem for the proposed multi-beam probing based multicast as

$$\mathcal{P}4: \max_{\Omega} \min_{\forall u} \left\{ \gamma_{u,\hat{b}}^{\Omega} \right\}$$
s.t. $\Omega \in (\mathcal{F})^{N_{\text{RF}}}$. (45)

Denote by $\lambda'_u = N_{\rm RF} \sigma^2/\mathsf{g}_u^2 \left| [a_{\rm rx}(\psi_u)]_{\hat{b}} \right|^2$ for $u=1,\cdots,N_{\rm UE}$ and $\lambda'_{\rm max}=\max\left\{\lambda'_1,\cdots,\lambda'_{N_{\rm UE}}\right\}$. Similar to (28), we obtain a lower bound of $\gamma_{u,\hat{b}}^\Omega$ as

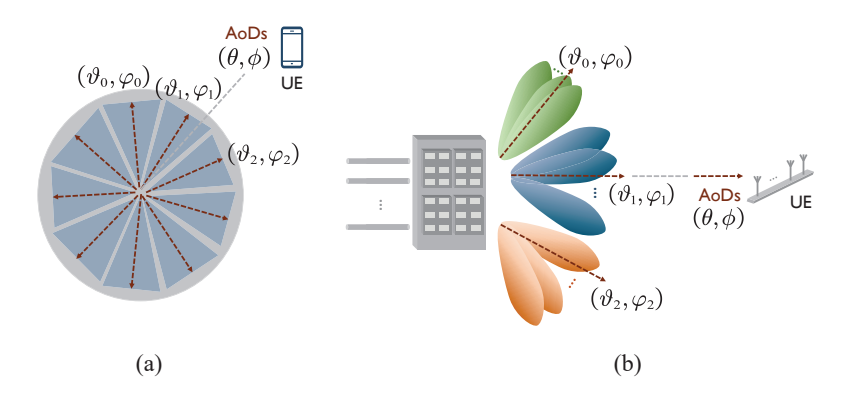
$$\dot{\gamma}_{u}^{\Omega} = \frac{\left|\mathbf{h}_{u}^{\Omega}\right|^{2}}{\lambda_{\max}' + \left[\frac{\left[\sigma^{2}\left(\left|\mathbf{h}_{u}^{\Omega}\right|^{2}/\lambda_{\max}'+1\right)\right]^{1/2}}{1-\xi_{\max}} - 1\right]\left(\left|\mathbf{h}_{u}^{\Omega}\right|^{2} + \lambda_{\max}'\right)},\tag{46}$$

such that

$$\dot{\gamma}_u^{\Omega} \le \gamma_{u,\hat{b}}^{\Omega}, \quad u \in \{1, \cdots, N_{\text{UE}}\}. \tag{47}$$

Based on (47), we reformulate (45) as

$$\mathcal{P}5: \max_{\Omega} \min_{\forall u} \left\{ \dot{\gamma}_{u}^{\Omega} \right\}$$
s.t. $\Omega \in \left(\mathcal{F} \right)^{N_{\mathrm{RF}}}$. (48)



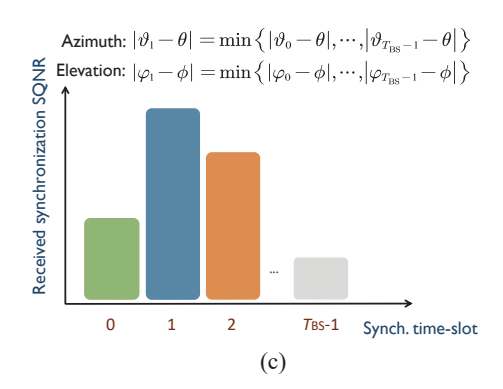


Fig. 6. (a) The anchor directions in the synchronization time-slot 1 best characterize the AoDs of the UE of interest. (b) The auxiliary beams formed for synchronization time-slot 1 best cover the UE of interest. (c) The UE of interest would experience the highest received synchronization SQNR when accessing to synchronization time-slot 1.

C. Design procedure of proposed multi-beam probing based approach

Similar to $\mathcal{P}3$ in (30), solving $\mathcal{P}5$ in (48) also requires the BS to have explicit knowledge of the channel directional information of all UEs, which is unavailable during the initial frame timing synchronization phase. In our proposed design, the UEs with significantly different AoDs are not supposed to synchronize to the network simultaneously, but instead via different synchronization time-slots. That is, for a given synchronization time-slot, we are only interested in a certain group of UEs that have similar AoDs. We therefore define an anchor direction to characterize those similar AoDs as much as possible for the synchronization time-slot of interest. As one synchronization frame contains $T_{\rm BS}$ synchronization timeslots, we define a set of $T_{\rm BS}$ anchor angular directions to represent the potential channel directions. We provide an example of the anchor direction for a given synchronization time-slot in Fig. 5(a). The anchor directions and $T_{\rm BS}$ synchronization timeslots have one-to-one mapping, and all $T_{\rm BS}$ anchor directions uniformly sample the angular range of interest, which is shown in Fig. 5(b). If the number of synchronization timeslots $T_{\rm BS} \to \infty$, the anchor directions fully sample the given angular space such that they characterize all possible channel directions. Note that other choices of the anchor directions are possible (e.g., non-uniformly sample the given angular space), depending on practical system requirements.

Based on the definition of anchor direction, we now reformulate the optimization problem in (48). We first define ϑ^* and φ^* as the azimuth and elevation anchor directions for the synchronization time-slot of interest and use them to represent the potential channel's azimuth and elevation AoDs. Note that this representation becomes more accurate as $T_{\rm BS}$ increases. Similar to (42), we first define

$$\mathbf{h}^{\Omega^{\star}} = \sum_{j=0}^{N_{\mathrm{RF}}-1} \left[\boldsymbol{a}_{\mathrm{tx}}^{*} \left(\vartheta^{\star} + \varphi^{\star} \right) \right]_{jN_{\mathrm{A}}+1:(j+1)N_{\mathrm{A}}} \boldsymbol{p}_{j}, \tag{49}$$

where Ω^* denotes the set of candidate beams with ϑ^* and φ^* as the corresponding azimuth and elevation anchor directions. Similar to (46), we can then obtain

$$\dot{\gamma}^{\Omega^{\star}} =$$

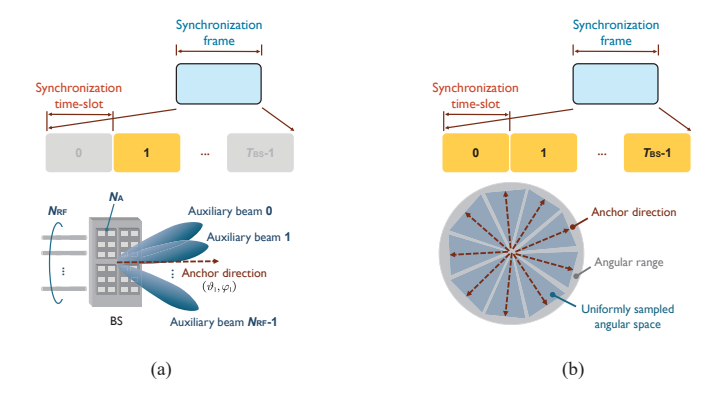


Fig. 5. (a) Conceptual examples of anchor direction and auxiliary beams for synchronization time-slot 0. (b) Across $T_{\rm BS}$ synchronization time-slots, all $T_{\rm BS}$ anchor directions uniformly sample the given angular space.

$$\frac{\left|\mathbf{h}^{\Omega^{\star}}\right|^{2}}{\lambda_{\max}' + \left[\frac{\left[\sigma^{2}\left(\left|\mathbf{h}^{\Omega^{\star}}\right|^{2}/\lambda_{\max}'+1\right)\right]^{1/2}}{1-\xi_{\max}} - 1\right]\left(\left|\mathbf{h}^{\Omega^{\star}}\right|^{2} + \lambda_{\max}'\right)}$$
(50)

According to (48), we formulate the optimization problem as

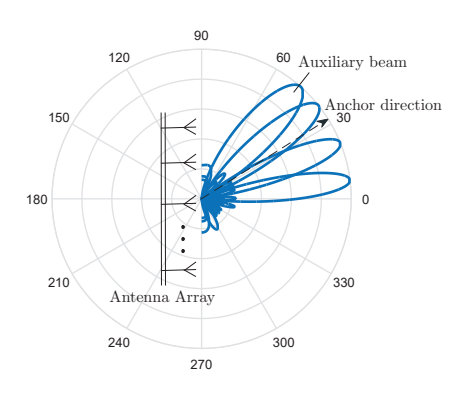
$$\mathcal{P}6: \max_{\Omega^{\star}} \left\{ \dot{\gamma}^{\Omega^{\star}} \right\}$$
s.t. $\Omega^{\star} \in (\mathcal{F})^{N_{\mathrm{RF}}}$,

which transforms the complex max-min optimization problem into a maximization problem. To solve (51), the BS can execute the exhaustive search over all possible combinations among the candidate beam codewords in \mathcal{F} , resulting in

$$\Omega_{\text{opt}}^{\star} = \underset{\Omega^{\star} \in (\mathcal{F})^{N_{\text{RF}}}}{\operatorname{argmax}} \left\{ \dot{\gamma}^{\Omega^{\star}} \right\}, \tag{52}$$

for the given synchronization time-slot. We refer to the simultaneously probed beams in $\Omega^{\star}_{\mathrm{opt}}$ as auxiliary beams for the synchronization time-slot of interest as depicted in Fig. 5(a). Through the auxiliary beams, the BS simultaneously samples multiple angles around a given anchor direction, and this process repeats for all T_{BS} anchor directions.

We now explain (52) using the conceptual example provided in Fig. 6. Consider synchronization time-slot 1 with the



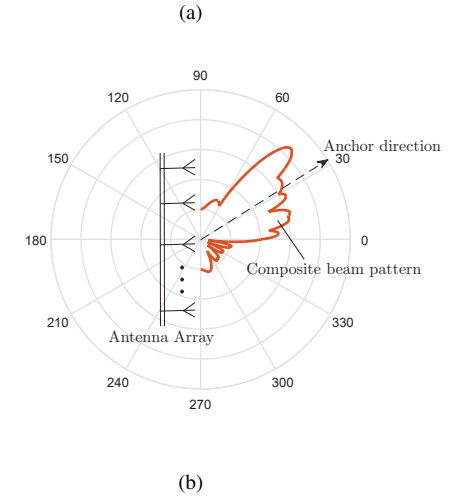


Fig. 7. An example of auxiliary beams is provided in (a); the corresponding composite beam is presented in (b).

corresponding azimuth and elevation anchor directions ϑ_1 and φ_1 in Fig. 6(a) and the corresponding auxiliary beams in Fig. 6(b). The main target of forming the auxiliary beams for synchronization time-slot 1 is to ensure that if a given UE's azimuth and elevation AoDs θ and ϕ are best characterized by ϑ_1 and φ_1 , i.e., $|\vartheta_1 - \theta| = \min \{|\vartheta_t - \theta|, t = 0, \cdots, T_{\rm BS} - 1\}$ and $|\varphi_1 - \phi| = \min \{|\varphi_t - \phi|, t = 0, \cdots, T_{\rm BS} - 1\}$, the UE would experience the highest received synchronization SQNR at zero-lag correlation when accessing to synchronization time-slot 1 among all synchronization time-slots (depicted by a conceptual plot in Fig. 6(c)).

From (39), (42) and (49), for the proposed multi-beam probing strategy with common synchronization signal structure, the simultaneously probed auxiliary beams actually form an effective composite beam. In Fig. 7, we provide examples of the auxiliary beams and the corresponding effective composite beam pattern. The auxiliary beams are selected from a discrete Fourier transform (DFT) beam codebook with oversampling factor of 2. Denoting the number of beam codewords in \mathcal{F} by $N_{\rm beam}$, we have $N_{\rm beam} = 2N_{\rm tot}$. In this case, we can determine the beam codebook resolution or the phase shifter resolution as $\log_2{(N_{\rm beam})}$ bits. As evident from Figs. 7(a) and 7(b), the effective composite beam may not yield the largest beamforming gain towards the corresponding anchor direction.

In summary, by optimizing the effective composite beam pattern via (52), we optimize the distribution/resolution of the input samples to the quantizer such that a high-resolution waveform is obtained to better trade off the beamforming gain and the resulted quantization distortion.

D. Impact of system specific parameters

By the definitions of λ'_{\max} and ξ_{\max} , i.e., $\lambda'_{\max} = \max\{\lambda'_1,\cdots,\lambda'_{N_{\mathrm{UE}}}\}$ and $\xi_{\max} = \max\{\xi_1,\cdots,\xi_{N_{\mathrm{UE}}}\}$, they still depend on each individual UE's SNR and quantization resolution. To avoid explicit feedback during the initial access, we define $\lambda'_{\mathrm{system}}$ and ξ_{system} as two system specific parameters to replace λ'_{\max} and ξ_{\max} in (51) in forming the auxiliary beams.

The system specific parameters can be determined by the BS or the network controller according to long-term measurements from previously connected UEs. Other design options of choosing appropriate system specific parameters are possible depending on practical implementation. If $\lambda'_{\rm system} \geq \lambda'_{\rm max}$ and $\xi_{\rm system} \geq \xi_{\rm max}$, the multi-beam optimization problem formulated in (51) is still valid. If $\lambda'_{\rm system} < \lambda'_{\rm max}$, $\xi_{\rm system} < \xi_{\rm max}$, and/or λ'_{u} and ξ_{u} ($u=1,\cdots,N_{\rm UE}$) vary significantly from UE to UE, the problem formulation in (51) becomes inaccurate. This in turn, may result in poor frame timing synchronization performance in the multi-user scenario. With the system specific parameters, we now summarize the overall procedure of our proposed low-resolution timing synchronization method in Algorithm 1 with complexity analysis for the key steps.

After the initial access, some form of feedback from the synchronized UE is beneficial to update the system specific parameters for future use. For instance, each individual UE can send its received SNR back to the BS in form of the channel quality indicator (CQI) to update $\lambda'_{\rm system}.$ The UE may also send its estimated azimuth and elevation AoDs $\hat{\phi}$ and $\hat{\theta}$, via the angle estimator developed in [27], back to the BS to further optimize the anchor angular directions. Note that it may not be always beneficial to update the system specific parameters by exploiting the feedback from the previously connected UEs. For instance, if the received SNRs for the previous and current UEs are significantly different due to the pathloss, the auxiliary beams obtained by using $\lambda'_{\mathrm{system}}$ (updated by the previous UEs) may not be suitable for the current UEs for low-resolution timing synchronization. In practice, the specific method used to configure the system specific parameters is subject to the implementation at the BS. In Section V, we used fixed values for the system specific parameters to characterize the worst-case scenario and evaluate our proposed method.

In the following, we discuss several other potential implementation options for our proposed low-resolution timing synchronization design. It is evident from (50), (51) and (52) that the selected auxiliary beams, and therefore the corresponding composite beam pattern, depend on the exact values of $\lambda'_{\rm system}$, $\xi_{\rm system}$, anchor angular directions, the beam codewords in \mathcal{F} , and how they contribute to the computation of γ^{Ω^*} . For instance, solving (51) assuming different $\xi_{\rm system}$'s (i.e., different quantization resolutions) may result in identical

auxiliary beams. One extreme example could be that the synchronization beam codebook \mathcal{F} contains only a single beam codeword. Hence, to better implement our proposed method in practice, it may be necessary to first analytically characterize the impact of different design parameters on the composite beam pattern. Further, if the system specific design parameters are dynamically configured by the network controller, there is a need to custom design a new synchronization beam codebook to reduce the beam search complexity in solving (51). For instance, the beam codewords in the new beam codebook can directly correspond to the composite beams shown in Fig. 7(b) and characterize many different combinations between λ'_{system} and ξ_{system} .

Algorithm 1 Procedure of multi-beam probing based lowresolution timing synchronization

BS-SIDE PROCESSING

1 : Configuring $\lambda'_{\mathrm{system}}$ and ξ_{system} based on long-term measurements and system statistics.

2 : **For** $t = 0, \dots, T_{BS} - 1$

Configuring anchor directions in both azimuth and elevation domains: ϑ_t and φ_t .

Formulating (50) using $\lambda'_{\mathrm{system}}$, ξ_{system} , ϑ_t and φ_t . Performing beam search/optimization according to (51). $\leftarrow - \mathcal{O}\left(\left(N_{\text{beam}}\right)^{N_{\text{RF}}}\right)$

Sending synchronization signal via the selected auxiliary beams according to (52).

7 : end For \leftarrow -- $\mathcal{O}\left(T_{\mathrm{BS}}\left(N_{\mathrm{beam}}\right)^{N_{\mathrm{RF}}}\right)$ 8 : Repeating Steps 1-7 N_{T} times in a periodic manner with period T_{period} .

 $\leftarrow -\mathcal{O}\left(N_{\mathrm{T}}T_{\mathrm{BS}}\left(N_{\mathrm{beam}}\right)^{N_{\mathrm{RF}}}\right)$ **UE-SIDE PROCESSING (UE** $u, u \in \{1, \cdots, N_{\mathrm{UE}}\}$)

i : Starting timing synchronization and collecting received signal samples.

ii : For $b=1,\cdots,M_{\mathrm{tot}}$ iii : Obtaining $\Gamma_{u,b}^{(0)}[\nu]$ by correlating the received signal samples with locally stored reference sequence via $\leftarrow - \mathcal{O}(N(N+1)(T_{\text{UE}}-1))$

iv : end For \leftarrow - $\mathcal{O}\left(M_{\mathrm{tot}}N(N+1)(T_{\mathrm{UE}}-1)\right)$

v: Selecting the receive antenna (\hat{b}) that has the highest correlation peak power $\left|\Gamma_{u,\hat{b}}^{(0)}[\hat{\nu}]\right|^2$.

vi : If $\left|\Gamma_{u\,\hat{b}}^{(0)}[\hat{\nu}]\right|^2 \geq \tau_{\rm corr}$

Estimating the timing position as $\hat{\nu}$. vii :

viii : Else

ix: Starting over from Step i.

x : end If

xi : After synchronization, sending necessary measurements such as the received SNR and channel estimates back to the BS to update the system specific parameters if needed.

V. NUMERICAL RESULTS

In this section, we evaluate the proposed multi-beam directional frame timing synchronization design for mmWave systems operating with low-resolution ADCs. The BS and UE employ a UPA and a ULA with inter-element spacing of $\lambda/2$ between the antenna elements. The BS covers three sectors, and each sector covers 120° angular range $[-60^{\circ}, 60^{\circ}]$ around azimuth boresight (0°) and 90° angular range $[-45^{\circ}, 45^{\circ}]$ around elevation boresight (0°). The UE monitors the entire 180° angular region $[-90^{\circ}, 90^{\circ}]$ around boresight (0°) . We assume a 125 MHz RF bandwidth with N=512 subcarriers. The corresponding CP length is D=64. We set the subcarrier spacing and symbol duration as 270 kHz and 3.7 μs following the numerology provided in [28]. The synchronization sequence occupies the central 63 subcarriers, and we set the DC-carrier as zero. We set the total number of receive antennas $M_{\rm tot}$ as 16 throughout the simulation section unless otherwise specified. Except in Fig. 9(b), we evaluate our proposed solution with the continuous subcarriers allocation strategy throughout this section. We set the correlation threshold $\tau_{\rm corr}$ as zero to detect the timing position. Other threshold values are possible depending on the actual channel condition [29], and they may result in different synchronization performances [30]. For the multi-user setup, we let $1/\lambda'_{\text{system}}$ be -20 dBunless otherwise specified. Further, we assume that the ADCs equipped at all UEs have identical quantization resolution (2) or 4 bits), which is used to determine the system specific quantization MSE ξ_{system} . Note that for a given ADC quantization resolution, we compute the corresponding quantization MSE according to [31, Table I].

In Fig. 8(a), we plot the cumulative density functions (CDFs) of the received synchronization SQNRs at zero-lag correlation for $N_{\text{tot}} = 32$ with $N_{\text{RF}} = 4$. We assume singlepath frequency-flat channels. We set the transmit SNR as 0 dB, which is calculated before the transmit beamforming and receive processing. We also examine the single-stream beamforming based directional frame timing synchronization method described in Section II with infinite-resolution (∞) and low-resolution (2 and 4 bits) ADCs for comparison. We construct the employed synchronization signals according to (1) with root index 34. As can be seen from Fig. 8(a), a significant performance gap can be observed between lowresolution quantization and infinite-resolution quantization for the existing strategy, though with increase in the quantization resolution, this performance difference decreases. By using the proposed multi-beam probing based design approach, the received synchronization SQNR performance is improved by several decibels in contrast to the single-stream beamforming algorithm. In Fig. 8(b), we provide the average received synchronization SQNRs at zero-lag correlation versus the quantization resolution of ADCs. In this example, we implement the statistical mmWave wideband channel model developed in [32] using the NYUSIM open source platform. The urban micro-cellular (UMi) scenario is assumed with non-line-of-sight (NLOS) components for 28 GHz carrier frequency. We evaluate both $N_{\mathrm{tot}} = 32$ and $N_{\mathrm{tot}} = 64$ for the proposed multi-beam probing and conventional single-

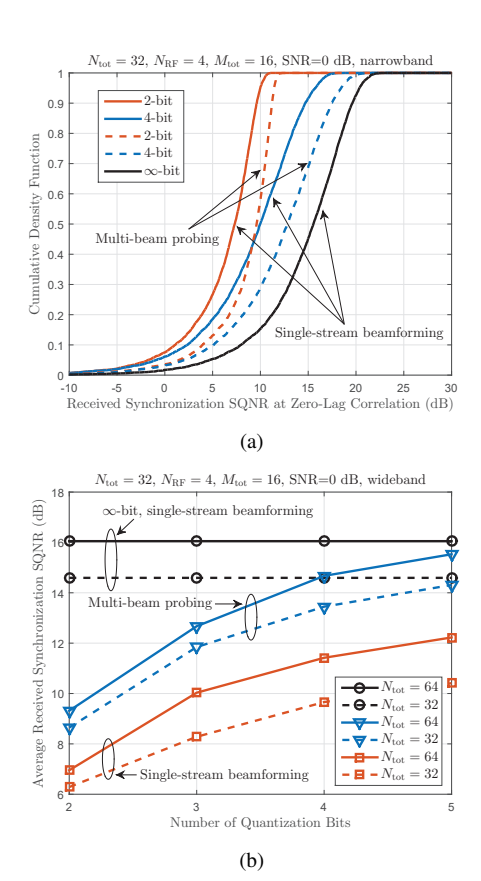


Fig. 8. (a) CDFs of the received synchronization SQNRs in single-path frequency-flat channels; $N_{\rm tot}=32$ with $N_{\rm RF}=4$. (b) Average received synchronization SQNRs versus the number of quantization bits in multi-path frequency-selective channels as in [32]; $N_{\rm tot}=32$ with $N_{\rm RF}=4$.

stream beamforming based designs. Similar to the narrowband results shown in Fig. 8(a), the proposed algorithm exhibits superior synchronization SQNR performance over the single-stream beamforming based design in wideband channels. Note that in both Fig. 8(a) and Fig. 8(b), we compute the SQNR results according to (19) and (44) for the single-stream and our proposed multi-beam probing based methods. The specific parameters in (19) and (44), e.g., the distortion factor of the quantizer and the beam pattern, are numerically obtained.

In Fig. 9(a), we evaluate the normalized MSE (NMSE) performance of the timing position estimate. Denoting the NMSE of the timing position estimate by $\omega_{\rm est}$, we have

$$\omega_{\text{est}} = \mathbb{E}\left[\left|\frac{\kappa_{\text{true}} - \kappa_{\text{est}}}{\kappa_{\text{true}}}\right|^2\right],$$
 (53)

where $\kappa_{\rm true}$ denotes the actual starting sample of an OFDM symbol (characterized by the first sample index of the synchronization signal), and $\kappa_{\rm est}$ corresponds to its estimated counterpart using various synchronization methods. We employ the wideband channels and randomly drop a total of 10 UEs within a circular cell having a 150 m radius. We obtain the NMSE performance of the timing position estimate over all UEs. It can be observed from Fig. 9(a) that the proposed multi-beam directional synchronization method with common synchronization signal design exhibits better performance than

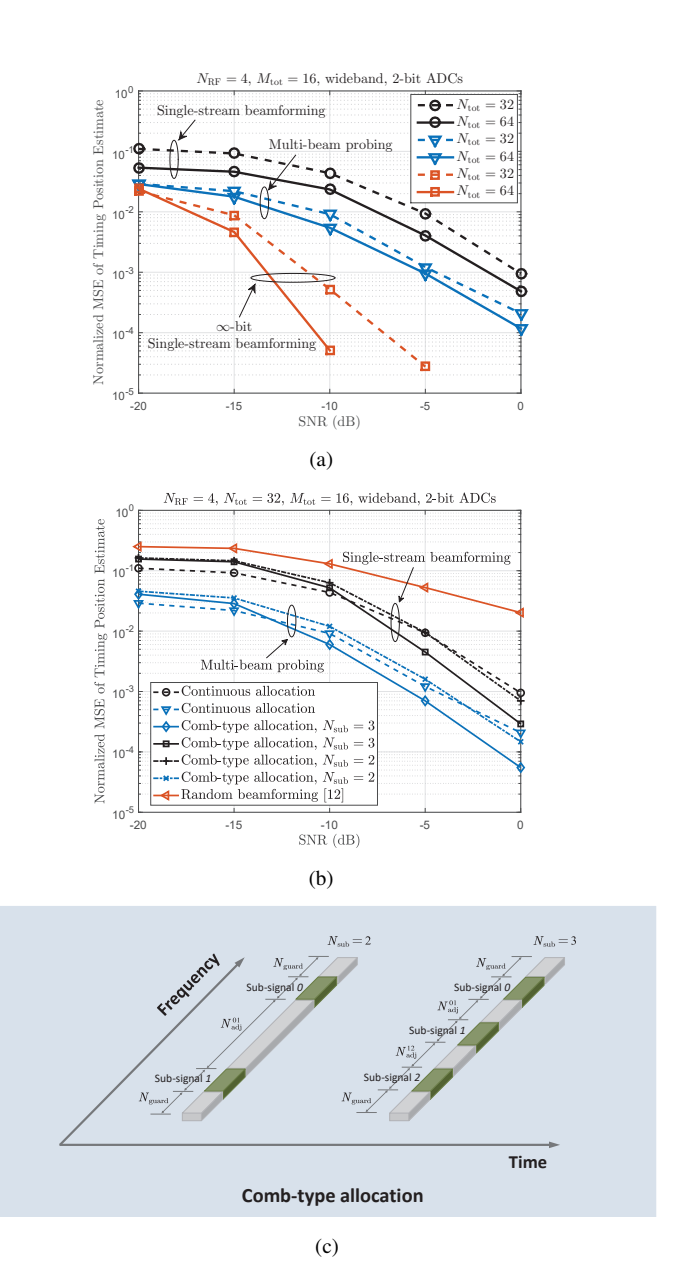


Fig. 9. Normalized MSE of timing position estimate versus SNR assuming multiple UEs equipped with 2-bit ADCs receivers. (a) Comparison between single-stream beamforming and multi-beam probing based methods. (b) Comparison among continuous and comb-type subcarriers allocation strategies, and the random beamforming based synchronization approach [12]. (c) Conceptual examples of comb-type subcarriers allocation for $N_{\rm sub}=2$ and $N_{\rm sub}=3$.

the single-stream beamforming based method. We can still observe some gap between our proposed method and the infinite-resolution case due to various design factors such as the number of UEs, the system specific parameters and the channel condition. For instance, at 10^{-3} NMSE of the timing position estimate, this performance gap is more than 5 dB SNR, implying that there is still room to further optimize our proposed approach.

In Fig. 9(b), we compare the two synchronization sequence allocation strategies in terms of the NMSE of the timing position estimate. Recall that $N_{\rm sub}$ represents the number of subsignals in a given synchronization time-slot. For $N_{\rm sub}=2$,

we first configure two guard bands with 65 subcarriers each located at both sides of a given frequency band (i.e., $N_{\rm guard} =$ 65 in Fig. 9(c)). We then assign the remaining subcarriers to two length-63 ZC sequences with $N_{\rm adj}^{01}=256$, depicted in Fig. 9(c). For $N_{\rm sub}=3$, we set $N_{\rm guard}=65$, $N_{\rm adj}^{01}=96$ and $N_{\rm adi}^{12} = 97$ assuming a total of 512 subcarriers and three length-63 identical ZC sequences. At relatively high SNR, the comb-type subcarriers allocation design with $N_{\rm sub}=3$ shows better performance than the continuous allocation and exhibits significant diversity gain for both the single-stream and our proposed multi-beam probing based methods. The comb-type allocation method with $N_{\text{sub}} = 2$, however, shows similar performance to the continuous allocation strategy in this example. Note that the performance of the comb-type assignment depends on the coherence bandwidth of the propagation channel, subcarrier spacing, $N_{
m sub}$, and the spacing between sub-signals. For mmWave frequencies, the coherence bandwidth is several tens of MHz at various frequency correlation levels [33], [34]. For the 270 kHz subcarrier spacing used in our simulations, the separation of the sub-signals for both of our $N_{\rm sub}=2$ and $N_{\rm sub}=3$ settings is greater than the coherence bandwidth for most of the correlation levels such that the frequency diversity gain can be better exploited. We also evaluate the random beamforming based design [12] in Fig. 9(b) for comparison. For the random beamforming, we assume that the $N_{\rm RF}$ simultaneously formed beams are randomly chosen from the employed DFT beam codebook with continuous subcarriers allocation for the synchronization signal. As the synchronization beams are not optimized for low-resolution quantization, the random beamforming based design even shows inferior NMSE performance of the timing position estimate than the single-stream beamforming based method.

For the last several examples, we numerically study the proposed method in a multi-cell scenario. Specifically, we assume 7 hexagonal cells and set the inter-site distance as 500~m. The root indices of the employed ZC sequences are 25, 29 and 34. The central cell corresponds to root index 25, and root indices 29 and 34 are reused among the other 6 surrounding cells such that the neighboring two cells are assigned two distinct root indices. Similar to the example provided in Fig. 9(b), we randomly drop a total of 10 UEs within each cell sector, and we set the minimum distance between the BS and UE as 20~m. We adopt the same path loss model as in [32] to conduct the performance evaluation. For a given BS-UE distance d, we express the path loss model as

$$PL_{\rm dB}(d) = PL_{\rm FS}(d_0) + 10\bar{n}\log_{10}\left(\frac{d}{d_0}\right) + \chi_{\sigma},$$
 (54)

$$PL_{\rm FS}(d_0) = 20\log_{10}\left(\frac{4\pi d_0}{\lambda}\right),\tag{55}$$

where $d_0=1$ m, \bar{n} is the path loss exponent, and χ_{σ} represents the log-normal random variable with 0 dB mean and standard deviation σ . The line-of-sight (LOS) probability is

$$P_{\text{LOS}}(d) = \left[\min\left(\frac{d_{\text{BP}}}{d}, 1\right) \left(1 - e^{-\frac{d}{\alpha}}\right) + e^{-\frac{d}{\alpha}}\right]^2, \quad (56)$$

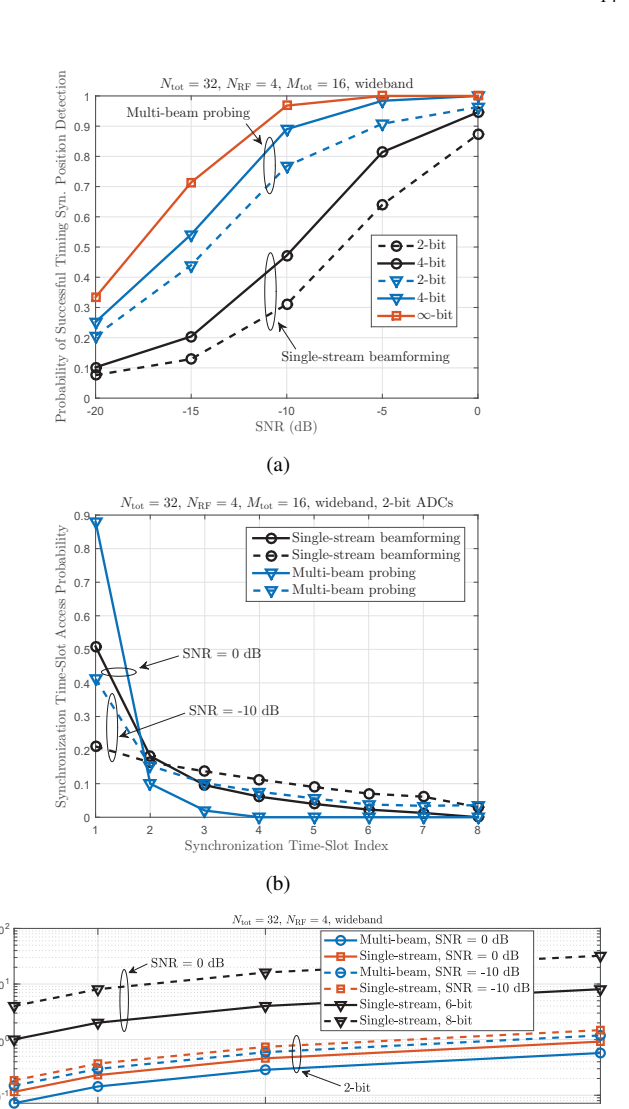


Fig. 10. A multi-cell scenario is assumed with a total of 7 hexagonal cells. A number of 10 UEs are randomly distributed within each cell sector with 2 or 4-bit ADCs. (a) Probability of successful timing position detection versus SNR. (b) Synchronization time-slot access probability versus synchronization time-slot index. (c) ADC power consumption for timing synchronization versus M_{tot} .

(c)

 M_{tot}

where $d_{\rm BP}=27~m$ and $\alpha=71~m$. For 28 GHz carrier frequency, we set \bar{n} and σ as 2.0 and 3.6 dB in LOS, and 3.4 and 9.7 dB in NLOS based on [32, Table III]. Performance statistics are obtained from the central cell of interest only. In Fig. 10(a), we evaluate the probability of successful timing position detection. Different from the NMSE of the timing position estimate, we calculate the probability of successful detection as $\Pr\left(\kappa_{\rm est}=\kappa_{\rm true}\right)$. It is observed that even at relatively low SNR, the proposed synchronization method with low-resolution ADCs can still achieve promising detection performance. For instance, at $-10~{\rm dB}$ SNR, the probability of successful detection is more than 0.8 for the proposed multibeam probing with common synchronization signal design.

In Fig. 10(b), we evaluate the synchronization time-slot access probability under low-resolution quantization. We cal-

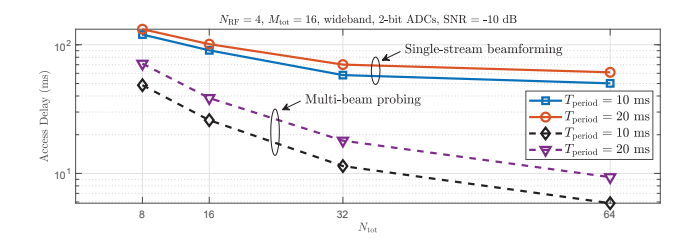


Fig. 11. A multi-cell scenario is assumed with a total of 7 hexagonal cells. A number of 10 UEs are randomly distributed within each cell sector with 2 or 4-bit ADCs. Access delay versus $N_{\rm tot}$.

culate the synchronization time-slot access probability based on the following procedure. If a given UE successfully detects the frame timing position during synchronization time-slot $\tau_{\rm t}$, the algorithm stops for the UE of interest. Otherwise, the algorithm continues in synchronization time-slot $\tau_t + 1$ and repeats the previous procedure. The synchronization time-slot access probability evaluates how fast a specific UE is capable of correctly detecting the frame timing position. Fig. 10(b) shows that even with 2-bit ADCs, the UEs can correctly detect the frame timing position during the first several synchronization time-slots by using the proposed method. In Fig. 10(c), we examine the ADC power consumption of our proposed timing synchronization strategy and compare it with high-resolution quantization design. We use the adopted ADC power consumption model as $P_{ADC} = FOM_W \cdot f_s \cdot 2^{b_q}$ [25], where $f_{\rm s}$ corresponds to the Nyquist sampling rate, $b_{\rm q}$ represents the number of quantization bits, and FOM_W is Walden's figureof-merit [35] and configured as 50 fJ/conversion-step in this example. In accordance with the synchronization time-slot access probability presented in Fig. 10(b), we calculate the ADC power consumption for timing synchronization (denoted as \bar{P}_{ADC}) as follows. For a given UE, $\bar{P}_{ADC} = 2M_{tot}P_{ADC}N\tau_t$. The simulation results plotted in Fig. 10(c) are obtained by averaging over all UEs. It is evident from Fig. 10(c) that the low-resolution timing synchronization can save tens of Watts in contrast to the high-resolution case, showing its full potential to reduce the power consumption and implementation costs.

In Fig. 11, we present the access delay performance for the timing synchronization under low-resolution quantization. We assume that (i) if a UE successfully detects the timing position, we drop another UE to the system for timing synchronization, (ii) we update the system specific parameters every 100 ms, and (iii) every UE can start the frame timing synchronization at any given time. It is evident from Fig. 11 that with a smaller array, and therefore a low-resolution beam codebook in our setup, the access delay largely increases especially for our proposed multi-beam probing based method under both $T_{\rm period}=10$ ms and $T_{\rm period}=20$ ms. This is because the low-resolution beam codebook limits the degree of freedom in finding good beam combination, i.e., auxiliary beams, that better solves (51).

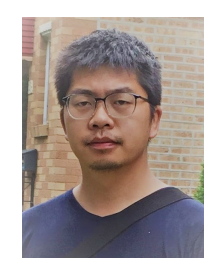
VI. CONCLUSIONS

In this paper, we developed and evaluated a multi-beam probing-assisted directional frame timing synchronization method for mmWave systems with low-resolution ADCs. We first formulated the optimization problem as maximizing the minimum received synchronization SQNR at zero-lag correlation among all UEs. We solved this problem by transforming the complex max-min multicast beamforming problem into a maximization problem. We then proposed a multi-beam probing strategy to tackle the maximization problem by optimizing the effective composite beam pattern. We showed via numerical examples that the effective composite beam can provide a good tradeoff between the beamforming gain and the quantization distortion and characterize the worst-case scenario of the network.

REFERENCES

- D. Zhu and R. W. Heath Jr., "Directional timing synchronization in wideband millimeter wave cellular systems with low-resolution ADCs," in 51st Asilomar Conf. on Signals, Systems, and Computers, Nov. 2017.
- [2] J. Wang, Z. Lan, C.-W. Pyo, T. Baykas, C.-S. Sum, M. Rahman, R. Funada, F. Kojima, I. Lakkis, H. Harada, and S. Kato, "Beam codebook based beamforming protocol for multi-Gbps millimeter-wave WPAN systems," *IEEE J. Sel. Areas Commun.*, vol. 27, no. 8, pp. 1390–1399, Oct. 2009.
- [3] R. W. Heath Jr., N. Gonzalez-Prelcic, S. Rangan, W. Roh, and A. Say-eed, "An overview of signal processing techniques for millimeter wave MIMO systems," *IEEE J. Sel. Top. Signal Process.*, vol. 10, no. 3, pp. 436–453, Feb. 2016.
- [4] A. Mezghani and J. A. Nossek, "Analysis of Rayleigh-fading channels with 1-bit quantized output," in *IEEE Intern. Symp. on Info. Theory*, Jul. 2008.
- [5] J. Singh, O. Dabeer, and U. Madhow, "On the limits of communications with low-precision analog-to-digital conversion at the receiver," *IEEE Trans. Commun.*, vol. 57, no. 12, pp. 3629–2639, Dec. 2009.
- [6] J. Mo and R. W. Heath Jr., "Capacity analysis of one-bit quantized MIMO systems with transmitter channel state information," *IEEE Trans. Signal Process.*, vol. 63, no. 20, pp. 5498–5512, Oct. 2015.
- [7] M. T. Ivrlac and J. A. Nossek, "Challenges in coding for quantized MIMO systems," in *IEEE Intern. Symp. on Info. Theory*, Jul. 2006.
- [8] B. M. Murray and I. B. Collings, "AGC and quantization effects in a zero-forcing MIMO wireless system," in *IEEE Veh. Tech. Conf.*, May 2006
- [9] "Evolved Universal Terrestrial Radio Access (E-UTRA); Physical Channels and Modulation," 3GPP TS 36.211, Apr. 2018. [Online]. Available: http://www.3gpp.org/ftp//Specs/archive/36_series/36.211/.
- [10] W. Roh et al., "Millimter-wave beamforming as an enabling technology for 5G cellular communications: theoretical feasibility and prototype results," *IEEE Commun. Mag.*, vol. 52, no. 2, pp. 106–113, Feb. 2014.
- [11] "NR; Physical Channels and Modulation," 3GPP TS 38.211, Jun. 2018. [Online]. Available: http://www.3gpp.org/ftp/Specs/archive/38_series/38.211/.
- [12] Y. Yang, H. S. Ghadikolaei, C. Fischione, M. Petrova, and K. W. Sung, "Fast and reliable initial access with random beamforming for mmWave networks," arXiv preprint arXiv:1802.06450, Nov. 2018.
- [13] C. N. Barati, S. A. Hosseini, S. Rangan, P. Liu, T. Korakis, S. S. Panwar, and T. S. Rappaport, "Directional cell discovery in millimeter wave cellular networks," *IEEE Trans. Wireless Commun.*, vol. 14, no. 12, pp. 6664–6678, Dec. 2015.
- [14] D. Zhu, R. Bendlin, S. Akoum, A. Ghosh, and R. W. Heath Jr., "Double-sequence frequency synchronization for wideband millimeterwave systems with few-bit ADCs," arXiv preprint arXiv:1812.03629, Dec. 2018.
- [15] N. Prasad, X. F. Qi, and A. Gatherer, "Optimizing beams and bits: a novel approach for massive MIMO base-station design," arXiv preprint arXiv:1810.07522, Nov. 2018.
- [16] A. Mezghani and R. W. Heath Jr., "MIMO beampattern and waveform design with low resolution DACs," arXiv preprint arXiv:1811.06451, Dec. 2018.

- [17] A. Mezghani and J. Nossek, "Capacity lower bound of MIMO channels with output quantization and correlated noise," in *IEEE Intern. Symp.* on *Info. Theory*, 2012.
- [18] J. J. Bussgang, "Crosscorrelation functions of amplitude-distorted Gaussian signals," Mar. 1952.
- [19] M. Giordani, M. Polese, A. Roy, D. Castor, and M. Zorzi, "A tutorial on beam management for 3GPP NR at mmWave frequencies," arXiv preprint arXiv:1804.01908, Apr. 2018.
- [20] B. M. Popovic, "Generalized chirp-like polyphase sequences with optimum correlation properties," *IEEE Trans. Inf. Theory*, vol. 38, no. 4, pp. 1406–1409, Jul. 1992.
- [21] Y. Tsai and G. Zhang, "Time and frequency synchronization for 3GPP long term evolution systems," in *IEEE Veh. Tech. Conf.*, May 2007.
- [22] D. Zhu, J. Choi, and R. W. Heath Jr., "Two-dimensional AoD and AoA acquisition for wideband millimeter-wave systems with dual-polarized MIMO," *IEEE Trans. Wireless Commun.*, vol. 16, no. 12, pp. 7890–7905, Dec. 2017.
- [23] C. Mollen, J. Choi, E. G. Larsson, and R. W. Heath Jr., "Uplink performance of wideband massive MIMO with one-bit ADCs," *IEEE Trans. Wireless Commun.*, vol. 16, no. 1, pp. 87–100, Jan. 2017.
- [24] K. Roth and J. A. Nossek, "Achievable rate and energy efficiency of hybrid and digital beamforming receivers with low resolution ADC," *IEEE J. Sel. Areas Commun.*, vol. 35, no. 9, pp. 2056–2068, Sep. 2017.
- [25] J. Mo, A. Alkhateeb, S. Abu-Surra, and R. W. Heath Jr., "Hybrid architectures with few-bit ADC receivers: achievable rates and energyrate tradeoffs," *IEEE Trans. Wireless Commun.*, vol. 16, no. 4, pp. 2274–2287, Apr. 2017.
- [26] K. Manolakis, D. M. Estevez, V. Jungnickel, W. Xu, and C. Drewes, "A closed concept for synchronization and cell search in 3GPP LTE systems," in *IEEE Wireless Commun. Netw. Conf.*, Apr. 2009, pp. 1–6.
- [27] D. Zhu, J. Choi, and R. W. Heath Jr., "Auxiliary beam pair enabled AoD and AoA estimation in closed-loop large-scale mmWave MIMO system," *IEEE Trans. Wireless Commun.*, vol. 16, no. 7, pp. 4770–4785, Jul. 2017.
- [28] Z. Pi and F. Khan, "An introduction to millimeter-wave mobile broadband systems," *IEEE Commun. Mag.*, vol. 49, no. 6, pp. 101– 107, Jun. 2011.
- [29] E. Zhou, Z. Zhang, and H. Kayama, "Precise timing synchronization algorithm for burst MIMO-OFDM transmission," NTT DOCOMO Technical Journal, vol. 19, no. 4, pp. 30–37, 2009.
- [30] M. H. Nassralla, M. M. Mansour, and L. M. Jalloul, "A low-complexity detection algorithm for the primary synchronization signal in LTE," *IEEE Trans. Veh. Tech.*, vol. 65, no. 10, pp. 8751–8757, Oct. 2016.
- [31] J. Mo, P. Schniter, and R. W. Heath Jr., "Channel estimation in broadband millimeter wave MIMO systems with few-bit ADCs," *IEEE Trans. Signal Process.* vol. 66, no. 5, pp. 1141–1154, Mar. 2018.
- Trans. Signal Process., vol. 66, no. 5, pp. 1141–1154, Mar. 2018.
 [32] M. K. Samimi and T. S. Rappaport, "3-D millimeter-wave statistical channel model for 5G wireless system design," *IEEE Transactions on Microwave Theory and Techniques*, vol. 64, no. 7, pp. 2207–2225, Jul. 2016.
- [33] P. M. Smulders, "Statistical characterization of 60-GHz indoor radio channels," *IEEE Trans. Antennas Propag.*, vol. 57, no. 10, pp. 2820– 2829, Oct. 2009.
- [34] J. Du and R. A. Valenzuela, "How much spectrum is too much in millimeter wave wireless access," *IEEE J. Sel. Areas Commun.*, vol. 35, no. 7, pp. 1444–1458, Jul. 2017.
- [35] R. H. Walden, "Analog-to-digital converter survey and analysis," *IEEE J. Sel. Areas Commun.*, vol. 17, no. 4, pp. 539–550, Apr. 1999.



Dalin Zhu received the B.Eng. in Information Engineering from Beijing University of Posts and Telecommunications (BUPT) and M.Sc. in Electrical and Computer Engineering from Kansas State University in 2007 and 2009, respectively. He obtained his Ph.D. degree in wireless communication and networking from The University of Texas at Austin in 2019. He is now a research staff engineer with Samsung Research America.

From 2010 to 2014, he worked as a research staff member and project manager in the Dept. of

Wireless Communications at NEC Laboratories China (NLC) focusing on 3GPP LTE/LTE-A standardization, TD-LTE system-level simulator development and C-RAN prototyping. From 2012 to 2013, he was a visiting scientist at the Wireless Systems Laboratory (WSL), Stanford University. From 2014 to 2015, he worked at Samsung R&D Institute China - Beijing (SRC-B) as a staff engineer working towards 5G related topics including new waveform design, massive MIMO, non-orthogonal multiple access schemes, and mmWave communications. During the summers of 2018, 2017 and 2016, he worked as an intern at AT&T Labs, Austin, TX and Huawei Technologies, Rolling Meadows, IL focusing on 5G new radio simulation and research.

Dr. Zhu was the recipient of the University Graduate Continuing Fellowship (2018-2019), Cullen M. Crain Endowed Scholarship in Engineering (2017-2018) from the University of Texas at Austin, Award of Excellence (2015/Q1) from Samsung R&D Institute China - Beijing, best paper award from Chinacom 2013 (Green Communications Symposium), and Dean's Special Award of Merit (2010-2011) from NEC Laboratories China.



Ralf Bendlin (S'07 - M'11) is a Principal Member of Technical Staff at AT&T Labs in Austin, Texas. Before joining AT&T Labs, he was a Senior Wireless Systems Architect with Intel Corporation in Portland, Oregon and a Systems Engineer with Texas Instruments Inc. in Dallas, Texas. He has worked on algorithm development, performance prediction, optimization, systems architecture, and technology strategy for current and next-generation wireless networks and has actively participated in the definition of several global communications standards

for which he holds several patents.

Dr. Bendlin earned a Bachelor's degree and a Master's degree from the Munich University of Technology in Munich, Germany as well as a Master's degree and a Ph.D. from the University of Notre Dame in South Bend, Indiana. All degrees are in Electrical Engineering and Information Technology. He is a member of the Industry Advisory Council of the Department of Electrical Engineering at the University of Notre Dame and the Technical Program Chair of the IEEE GLOBECOM 2019 Workshop on High-Dimensional, Low-Resolution Architectures for Power-Efficient Wireless Communications. He has previously served as the Technical Program Chair of the 2017 IEEE International Symposium on Dynamic Spectrum Access Networks, as Guest Editor of the IEEE Transactions on Cognitive Communications and Networking (TCCN), and as a member of the Advisory Council of the College of Engineering at the University of Notre Dame.



Salam Akoum (S'07 - M'13) is a principal member of technical staff at AT&T labs, advanced radio technology group. She is an active contributor to 3GPP 5G standardization, responsible for specifications of the physical layer of the radio interface. Salam works on algorithm development and system architecture and optimization for current and next-generation wireless networks. Prior to joining AT&T labs, Salam worked at the center for Social Innovation at Hitachi America R&D, where she investigated connectivity solutions, analytics and traffic

optimization for IT and OT convergence and received the Hitachi above and beyond award in 2014.

Dr. Akoum earned her Ph.D. in Electrical Engineering from the University of Texas at Austin in 2012. She graduated with a Bachelor of Engineering in Computer and Communications Engineering and a minor in Mathematics (Honors) from the American University of Beirut, Lebanon in 2006, and completed her Master of Science in Electrical Engineering from the University of Utah in 2008. She was a visiting researcher at SUPELEC, France in 2011.



Robert W. Heath Jr. (S'96 - M'01 - SM'06 - F'11) received the B.S. and M.S. degrees from the University of Virginia, Charlottesville, VA, in 1996 and 1997 respectively, and the Ph.D. from Stanford University, Stanford, CA, in 2002, all in electrical engineering. From 1998 to 2001, he was a Senior Member of the Technical Staff then a Senior Consultant at Iospan Wireless Inc, San Jose, CA where he worked on the design and implementation of the physical and link layers of the first commercial MIMO-OFDM communication system. Since Jan-

uary 2002, he has been with the Department of Electrical and Computer Engineering at The University of Texas at Austin where he is a Cullen Trust for Higher Education Endowed Professor, and is a Member of the Wireless Networking and Communications Group. He is also President and CEO of MIMO Wireless Inc. He authored "Introduction to Wireless Digital Communication" (Prentice Hall, 2017) and "Digital Wireless Communication: Physical Layer Exploration Lab Using the NI USRP" (National Technology and Science Press, 2012), and co-authored "Millimeter Wave Wireless Communications" (Prentice Hall, 2014).

Dr. Heath has been a co-author of sixteen award winning conference and journal papers including the 2010 and 2013 EURASIP Journal on Wireless Communications and Networking best paper awards, the 2012 Signal Processing Magazine best paper award, a 2013 Signal Processing Society best paper award, 2014 EURASIP Journal on Advances in Signal Processing best paper award, the 2014 Journal of Communications and Networks best paper award, the 2016 IEEE Communications Society Fred W. Ellersick Prize, the 2016 IEEE Communications and Information Theory Societies Joint Paper Award, and the 2017 Marconi Prize Paper Award. He received the 2017 EURASIP Technical Achievement award. He was a distinguished lecturer in the IEEE Signal Processing Society and is an ISI Highly Cited Researcher. In 2017, he was selected as a Fellow of the National Academy of Inventors. He is also an elected member of the Board of Governors for the IEEE Signal Processing Society, a licensed Amateur Radio Operator, a Private Pilot, a registered Professional Engineer in Texas.



Arun Ghosh received his PhD from University Illinois at Urbana-Champaign (98) and his masters and bachelors from Indian Institute of Technology Kanpur (92). He is currently the Director of Advanced Wireless Technology Group at AT&T Labs, where he is responsible for the research and development of advanced wireless technology for 5G and beyond 5G Wireless Networks. Currently he is involved in the development of many new technology concepts for beyond 5G mobile networks as they relate to mmWave communication systems, massive MIMO

systems, mobile multi-hop network, low resolution ultra-massive MIMO systems, network coding etc. He is also widely recognized as the key innovator behind many revolutionary new concepts for 5G such as IAB (integrated access and backhaul), Asynchronous Multi-Point Transmission, Spatial Compression for 5G Fronthaul. His main area of research relates signal processing and communication theory but he has also worked extensively on other topics such as cloud RAN, advanced system architecture and has published extensively in these area and is a key contributor to AT&T patent portfolio on this subject. Dr. Ghosh is the recipient of the AT&T Fellow Award and has also authored several bestselling books on LTE and WiMAX.